A MACRO-STRUCTURAL CHARACTERISTIC OF BRAIN WHITE MATTER: 'DISPERSION' WITH ITS CLINICAL AND TECHNICAL APPLICATIONS

by

Ali Demir

B.S. in Computer Science and Engineering, Yeditepe University, 2008

B.S. in Biomedical Engineering, Yeditepe University, 2008

M.S. in Electronics Engineering, Sabancı University, 2010

Submitted to the Institute of Biomedical Engineering

in partial fulfillment of the requirements

for the degree of

Doctor

of

Philosophy

Boğaziçi University

2020

ACKNOWLEDGMENTS

I would like to thank first my supervisors Prof. Mehmed Özkan and Assoc. Prof. Aziz Uluğ for their support that it started when I was in Yeditepe University. At that time, Prof. Aziz Uluğ motivated and supervised me to study diffusion MRI in my graduation project and Prof. Mehmed Özkan co-supervised me with a great support as a visiting professor. I will always remember those great times that I was using skype to reach Prof. Aziz Uluğ without any hesitation, and waiting at the door of a class of Prof. Mehmed Özkan to demonstrate what I have done as a progress. I'm deeply grateful for their lifelong support so that I could now have this opportunity to express my gratitude for obtaining the PhD degree with the help of their supervision.

I also would like to thank Assoc. Prof. Esin Öztürk Işık for the guidance through the progress meetings to improve the quality of my thesis with very precious advises that I will remember and keep those within my mind for the next projects. Besides, I'm very grateful for her kindness and support even in times that she was completely busy within her schedule.

It is a pleasure that my thesis was examined by Prof. Kubilay Aydın, Prof. Koray Çiftçi and Prof. Ahmet Ademoğlu. I appreciate their motivating comments and mind-opening questions which will guide me for the upcoming extensions of my thesis work.

I'm very pleased to have very nice BME mates Ahmet Atasoy, Shavkat Kuchimov, Mehmet Turpçu, Ersin Topbaş, Munzer Alseed, Hasan Şahin, Gülfize Sava, İpek Karakuş, and Seda Dumlu. Those were the great times with very nice conversations and happy hours.

I would specially thank to Prof. Mohammad Alsunaidi for his great friendship and kindness that he proofread our recent journal paper with a great intention to help.

I would also thank to Şeyma Gezen Kanacı and Emre Kanacı for their kindness and support with the very last cross-checks and their pinpoint advises.

I also thank to my mother Hanım Demir, father Hüseyin Demir, and brothers Musa and Mustafa Demir for their valuable presence and precious support with all their heart.

This thesis is dedicated to my lovely wife Mukadder Gezen Demir for her endless cheeriness and strong patience which keep me always on my way beyond all. It was all possible with her enthusiastic support.

This study was supported by TUBITAK 2211-C Scholarship. This work was also supported in part by EU 7th framework - TUBITAK Co-Funded Brain Circulation Scheme 2236 grant 291762/112C003.

ACADEMIC ETHICS AND INTEGRITY STATEMENT

I, Ali Demir, hereby certify that I am aware of the Academic Ethics and Integrity Policy issued by the Council of Higher Education (YÖK) and I fully acknowledge all the consequences due to its violation by plagiarism or any other way.

Name :

Signature:

Date:

ABSTRACT

A MACRO-STRUCTURAL CHARACTERISTIC OF BRAIN WHITE MATTER: 'DISPERSION' WITH ITS CLINICAL AND TECHNICAL APPLICATIONS

The main goal of this thesis is to find distinct macro-structural characteristics of brain white matter in the case of psychosis, where development of diagnostic imaging measures is necessary for early diagnosis and prospective studies. Given a tractogram data, which is a dense set of white matter fiber pathways of the whole brain obtained from diffusion magnetic resonance imaging, we propose to compute a global measure of dispersion for a voxel from the end point statistics of a set of fibers, which indicates complexity of the white matter voxel not locally but at macro scales. The findings on phantom data demonstrate sensitivity of the proposed measure to the tuning parameters and show its range characteristics. The findings on the real data demonstrate that proposed macro-structural dispersion information is found to be significant for discrimination of the schizophrenia and the bipolar patients from the healthy controls, especially when the frontally associative bundles such as cingulum and inferior occipito-frontal fasciculus are considered. The macroscopic dispersion measure is as informative as the local diffusion measures for the detection of changes in the white matter regions due to the psychosis. Beside, as a technical application, the dispersion map is considered and experimented for segmentation of cingulum. The findings of the thesis provide that the proposed measure is a potential diagnostic imaging marker in the case of psychosis and we contribute to the field of diagnostic research by generating a novel dispersion map of the brain that could be used for other clinical and technical applications.

Keywords: Brain white matter, macroscopic dispersion, tractogram, bipolar, schizophrenia.

ÖZET

BEYİN BEYAZ CEVHERİNİNİN BÜYÜK ÖlÇEKTE BİR YAPI ÖZELLİĞİ OLAN 'YAYILIM' ÖLÇÜTÜNÜN KLİNİK VE TEKNİK UYGULAMALARI

Bu tezin temel amacı beyaz cevher yolaklarının büyük ölçekteki karakteristik özelliklerini bularak psikoz vakalarının teşhis ve takibinde başvurulabilecek bir teşhis ölçütü ortaya çıkarmaktır. Beyaz cevher yolakları difüzyon ağırlıklı manyetik rezonans görüntülerinin işlenmesi ile ortaya çıkan "traktogram"da beyindeki yolakların bütününü kapsayacak şekilde oluşturulabilir. Tractogram verisini kullanarak, voksel boyutundaki sınırdan bağımsız, yani büyük ölçekte bir özellik olarak beyaz cevher yolaklarının karmaşıklık derecesinin ölçülebileceği bir yayılım ölçütü bu tez kapsamında önerilmiştir. Sentetik veriler üzerinde yaptığımız çalışmalar önerilen ölçütün bağımlı olduğu değişkenlere olan duyarlılığını göstermektedir. Önerilen büyük ölçekli yayılım ölçütünün şizofreni ve bipolar vakalarının normallerden farklı yayılım karakteristiklerine sahip olduklarını gösteren ayırt edici bir ölçüt olduğu gösterilmiştir. Önerdiğimiz büyük ölçekli yayılım ölçütü ile frontal beyin lobu ile bağlantılı olduğu bilinen singulum ve inferior oksipito-frontal fasikülleri özel olarak incelendiğinde bu farklılık ortaya çıkmaktadır. Bu yayılım ölçütü, voksel sınırları içerisinde ölçülmüş olan difüzyon ölçütleri kadar etkili bir ölçüt olduğu karşılaştırmalarla anlaşılmıştır. Önerilen ölçüt ile oluşturulmuş yayılım haritası ile teknik uygulama da yapılabilmiş ve örnek olarak singulum bölütleme çalışması yapılmıştır. Bu tezin sonuçları ışığında büyük-ölçek yayılım ölçütü ile oluşturulan beyin haritalarının psikoz vakalarının teşhisinde kullanılabilecek bir nörobelirteç olma olasılığı ortaya çıkmıştır. Önerilen yöntem farklı klinik durumlar için de sınanabilir ve teknik uygulamalarda yeni ilerlemeler sağlanabilir.

Anahtar Sözcükler: Beyin beyaz cevheri, büyük-ölçek yayılım, tractogram, bipolar, şizofreni.

TABLE OF CONTENTS

LIST OF FIGURES

LIST OF TABLES

LIST OF SYMBOLS

$S(ij)$	Signal intensity of magnetic relaxation in direction (ij)
D_{ij}	3 by 3 symmetric diffusion tensor
b_{ij}	Gradient strength in direction (ij)
λ_i	i^{th} eigenvalue of the diffusion tensor
$\boldsymbol{v_i}$	i^{th} eigenvector of the diffusion tensor
$Y_l^m(\mathbf{u})$	Spherical harmonic (SH) basis functions
$c_{l,m}$	Coefficients of each SH basis function
r	Radius of sphere ROI to select fibers of a voxel
R	Radius of truncation sphere
X_i	i^{th} fiber of a set
$x_{i,n}$	n^{th} point coordinate of the i^{th} fiber
m	Number of points on the fiber
$X^{(s)}$	Set of start points of a fiber
$X^{(e)}$	Set of end points of a fiber
$x_c^{(s)}$	Centroid of start point coordinates
$x_c^{(e)}$	Centroid of end point coordinates
$\sigma^{2(s)}$	Variance of the start point coordinates
$\sigma^{2(e)}$	Variance of the end point coordinates
δ_p	Macroscopic dispersion for the point p
C_t	An active contour at time step t
$g(\mathrm{I})$	Speed image obtained from the gradient of the image I
κ	Mean curvature of the contour
$\overrightarrow{\eta}$	Normal vector of the contour
G_i	Gaussian process representation of the i^{th} fiber
δ_g	Gaussian process based dispersion

LIST OF ABBREVIATIONS

WM	White matter
dMRI	Diffusion magnetic resonance imaging
DAIs	Diffusion anisotropy indices
MRI	Magnetic resonance imaging
FA	Fractional anisotropy
ADC	Apparent diffusion coefficient
MD	Mean diffusivity
RD	Radial diffusivity
ROI	Region of interest
SLF	Superior longitudinal fasciculus
AD	Axial diffusivity
ODF	Orientation distribution function
SH	Spherical harmonic
FOD	Fiber orientation density
SIFT	Spherical-deconvolution informed filtering of tractogram
FSL	FMRIB software library
BET	Brain extraction tool
JHU	ICBM-DTI-81 white-matter atlas
MNI	Montreal Neurological Institute
HC	Healthy control
BP	Bipolar
SCH	Schizophrenia
ANOVA	Analysis of variance
HCP	Human Connectome Project

1. INTRODUCTION

Quantitative characterization of the white matter (WM) circuitry in the human brain is paramount for mapping the structural connectivity, which is known to be affected by neurological diseases. Many countries including US, EU, and China devoted their attention and resources to resolve the structural and functional connection diagram of brain [1]. These initiatives motivate researchers from different disciplines to develop novel approaches to understand the anatomy and the function of the brain. Variety of review articles are published emphasizing the need of computational efforts to obtain a large scale circuit reconstruction of the brain, called connectome [1–10].

Diffusion magnetic resonance imaging (dMRI) can describe brain circuitry in vivo by measuring variations of water diffusion in several directions. In particular, these measurements provide insights into the mathematical representations of diffusion (e.g., diffusion tensors [11], higher-order tensors [12], orientation distribution functions [13]), which reflect the local fiber orientation profile. These representations can be used to extract a tractogram, i.e., a dense set of white matter (WM) fiber pathways of the whole brain computed using tractography algorithms [14], [15]. Once the information on the WM circuitry is inferred it is common to focus on selected fiber bundles (i.e., spatially coherent collections of fiber pathways), whose integrity is anticipated to be affected by development, degeneration, or disease [16]. Examples include brain tumors which can displace or infiltrate WM tracts, callosal atrophy (i.e., gradual loss of fibers forming the corpus callosum) in individuals with Alzheimer's disease [17], or diffusely abnormal WM (i.e., regions with reduced mild MRI hyper-intensity and ill-defined boundaries) linked to the pathogenesis of multiple sclerosis [18].

Representing fibers and quantifying fiber similarity play a fundamental role. Earlier approaches often employ shape descriptors/statistics [5], [19], [20] or point sequence-type parameterization along with the Chamfer or Hausdorff distances [21], [22], [23]. Although these methods yield promising results, their performance drops

when analysing partially overlapping or locally diverging fibers.

Fiber clustering and parcellation of large scale regions are two main approaches that produce quantitative descriptions of the brain's wiring diagram. Both methods are complementary ways for mapping the brain in different scales [2], [8], [24]. Structural information derived from dMRI and the functional information derived from resting state functional MRI combine and form a basis for most of the studies that aim to achieve a connectome [4], [7]. However, deriving a truly anatomically correct connectome may not be possible [3], [25]. A tractogram obtained using advanced tractography methods contains a considerable amount of fibers that do not reflect real underlying anatomy [4]. To overcome this issue, Fillard et al. proposed spin glass tractography method [26]. Knowing that the tractography is an ill-posed problem, Mangin et al. suggest that global modelling of the connectome can provide qualitative improvements to the tractogram [25]. Other issues, such as scale, stability, structural plasticity, and different localization of structure-function relationship, remark that each individual wired up differently and it is impossible to produce a definitive map of the human connectome [1], [9].

Specific attributes and motifs in the underlying structure of the brain characterize the neurobiological meaning of the parameters. WM microstructure is expressed in terms of diffusion anisotropy indices (DAIs) obtained from dMRI, such as fractional anisotropy (FA), apparent diffusion coefficient (ADC), mean diffusivity (MD), and radial diffusivity (RD) [27]. Several other indices which are sensitive to the surface and volume changes of the diffusion tensor [28] were also defined. Starting from the clinical use of dMRI, these indices are heavily employed as a marker for clinical disorders in the WM [29]. Region of interest (ROI) based tractography can be used to obtain the DAI statistics of a certain WM tract [30]. Moreover, atlas based studies lead to more advanced approaches, such as tract based spatial statistics and voxel based morphometry, which facilitate voxel-wise comparison of DAI statistics on the template space [31].

The new approaches are necessary for the statistical analysis of brain network data [9]. Prospectively, the tractogram of a brain is used to explore neural connections

to extract new statistics or markers for WM alterations. Most of the previous studies of WM indices derived from diffusion data are based on the local diffusion profile within a voxel. Furthermore, macroscopic motifs of the fibers have currently been considered as a potential biomarker for the changes along the WM fibers [32], [33]. In the light of aforementioned studies, we prospect that coherence or dispersion profiles [34], [35], [36] of the fibers passing through a voxel could be used as a biomarker at the macroscopic scale. The proposed inference has been investigated for the bipolar disorder that the next subsection is dedicated to our clinical motivation and its relevance to the proposed method.

1.1 Clinical Relevance and Motivation

Investigation of brain network characteristics of psychiatric cases using functional and structural brain mapping techniques become a clinical research focus for many recent studies [37], [38]. These studies show that the quantification of change or deformation in the brain WM caused by development or disease is a significant task. For quantification of the dMRI, at first glance, microstructural characteristics, such as fractional anisotropy and mean diffusivity, are considered as a biomarker for detecting anomalies. In the latter stages, the use of higher-order diffusion models and diffusion acquisition in many directions reduced estimation errors and increased the level of WM detail at microscopic scales. On the other hand, at macroscopic scales, a typical tractogram of the whole brain contains at least a hundred thousand fibers. Currently, manual seed ROI based filtering and fiber clustering approaches are used in combination to delineate a specific bundle of interest, and quantitative evaluation of the microstructural diffusion characteristics is performed for the delineated bundle. In fact, a tractogram is mostly considered as a data source for qualitative visualization of structural information at macroscopic scales [39].

In this thesis, we show that the qualitative information of tractogram could be quantified and mapped by the definition of a macroscopic feature for a given set of fibers. Specifically, knowing that the brain dynamics depend on the complex neural

connections [40], we demonstrate that the fiber motifs, passing through a voxel or a very small ROI (radius $\sim$ 1 mm), could be analyzed for macroscopic connection characteristics at a WM tissue that the ROI is centered. Hence, statistical measures derived from these fiber motifs would provide a novel bio-marker specifically computed for each voxel. Once a nearly perfect tractogram is obtained, the 3D profile of fibers passing through a small ROI centered at each voxel could be employed to compute macroscopic characteristics, such as dispersion. As a result, similar to an FA map, a novel dispersion map of the brain could be obtained. The proposed method includes also a methodological preprocessing framework (Section 4.2) for the spatial normalization and generation of the tractogram, which is fed as an input for dispersion quantification. Developed quantitative maps are applicable for pre-post and group-wise clinical studies.

2. BACKGROUND

2.1 Macrostructure of the Brain

The structure and function of the human brain have been studied throughout the history that we know the earliest written document was a papyrus paper found in Egypt dated to 17^{th} century B.C. [41]. It was originally written at least a thousand years earlier by a battlefield surgeon who described the clinical observations of head injuries carefully . Since then, now we know much more about our brain that it functions through electrical nerve impulses and has a full sense and control over each part of the body. Besides, it is the center of intelligence controlling our decisions, thoughts, and emotions that in other species it is not as developed as such. It is considered as a paradox that we use the brain to understand itself.

Having plenty of theoretical and technological advances in molecular and imaging sciences, we have explored many aspects of the structure of the brain and we know certain functioning mechanisms in terms of some chemicals and kinetics of the body. However we still do not have a complete understanding of how the brain functions with this structure and what are the structural or functional characteristics of the brain disorders. Since the motivation of this thesis focused on a macroscopic characteristic of the brain white matter, we will be introducing the gross neuroanatomy with limited information about the function and microscopic characteristics of the neural tissues.

Brain is a sensitive and vulnerable organ that is protected by several layers including the skull and cerebrospinal fluid. Soft tissue of the brain actually swims in a pool which is filled up with cerebrospinal fluid and the brain's soft structure is preserved within this fluid. Building block of the brain is a nerve cell or so called neuron, which has three different parts: cell bodies, axons, and dendrites. Surface of the brain is a thin layer of gray matter structure called cortex. It is mainly formed by the cell bodies of the neurons. Behind the gray matter layer, axons of the neurons form fibrous and

densely myelinated tissue layer which is brighter than the gray matter, therefore this layer is called white matter. These myelinated axons unite in groups of fibers and run forward to conduct impulses between cell bodies and dendrites of the neurons (Figure 2.1). Once the brain is sliced, the white matter tissue is mostly imaged to have a similar and homogeneous color, but in terms of the direction of the axonal pathways there are heterogeneous white matter regions if there are crossing, bending, or fanning fibers.

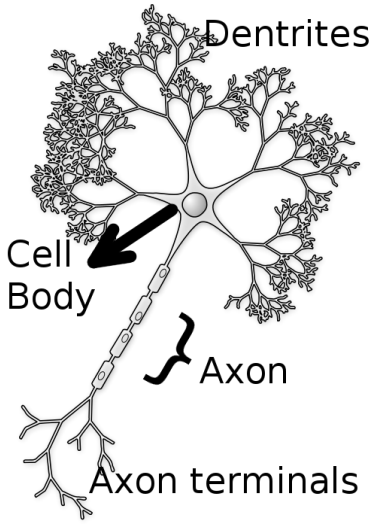

Figure 2.1 A schematic diagram of the nerve cell or neuron. Adopted from the internet [learnabout-parkinsonsdisease.wordpress.com].

Each fiber bundle forms gross nerve connections between distant sites with a unique geometric structure in cerebral white matter. The white matter fiber bundles are anatomically oriented in a sophisticated and complex network yet to attract many scientists to explore the role of these wonderfully oriented white matter fibers in brain functioning mechanisms. In vivo and ex vivo imaging techniques are developed in time to observe structural details of the white matter tissue and its functionality. Diffusion contrast of magnetic resonance imaging could be considered as a gold standard for in vivo imaging of the brain white matter fibers and sophisticated diffusion models are used to reconstruct fibers which depicts structural deviations within the white matter using 3D renders of the reconstructed pathways (that certain methods of diffusion MRI will be introduced in next section) . However, considering the resolution of the imaging, microscopic evaluation of the post-mortem brains provide more precise and

reliable images for the investigation of anatomical organization of the white matter connectivity in the nervous system.

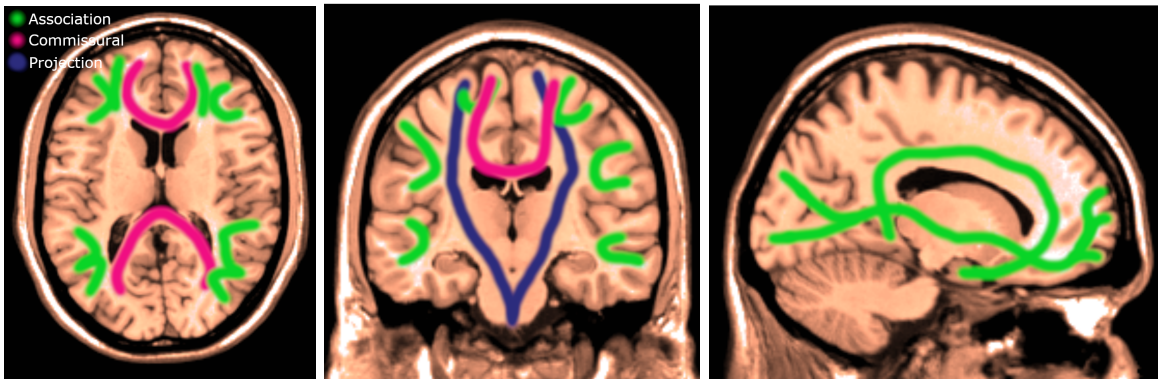

Figure 2.2 A schematic diagram showing commissural, association and projection fibers.

In this section, a brief overview is written describing the neuroanatomy of the long white matter fibers grouped by the location of the connected regions: (i) Commussiral fibers connect the left and right cerebral hemispheres passing through the mid sagittal section. (ii) Association fibers connect different gray matter regions within the hemisphere. (iii) Projection fibers connect cortex with mid-brain (diencephalon) regions such as thalamus and amygdala. Some projection fibers might reach up to the spinal cord. Images of the certain white matter bundles are adopted from cited works to demonstrate how they are observed in photographs of carefully dissected post-mortem brains using microsurgical techniques [42].

The greatest group of fibers in the brain is called corpus callosum that includes a collection of connected giant span of U shaped fibers along approximately half of the cerebral hemispheres and run between the left and the right hemispheres. Median sagittal section of the brain shows its central position and size. Anterior part of the corpus callosum is called the genu or forceps anterior (minor). These fibers could best be viewed in the axial section of the brain and connect the left and right frontal lobes. Central part is called the body of the corpus callosum that these fibers mostly run towards the superior regions of the cortex. Preserving their likewise U shape and keeping their center on the mid sagittal slice, the fibers of corpus callosum continues till the posterior part which is called splenium or forceps posterior (major) that these

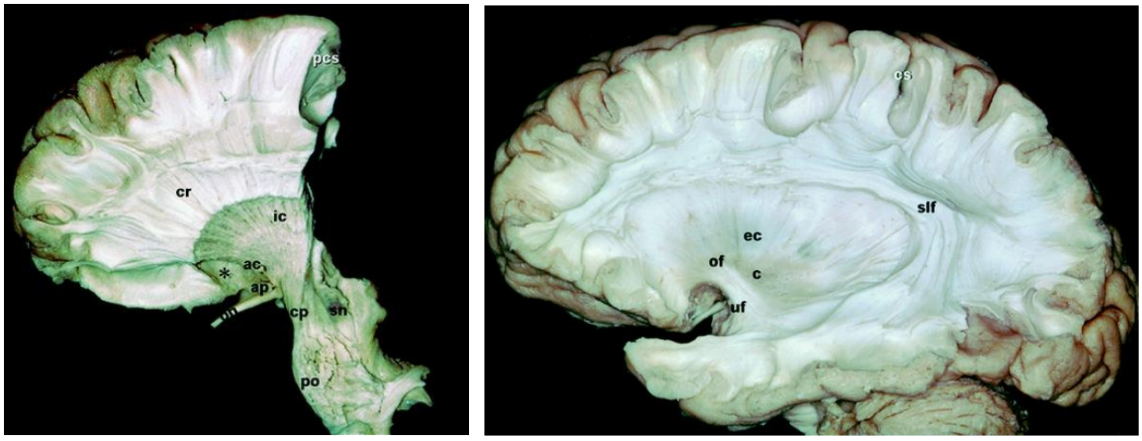

(a) (b)

Figure 2.3 Adopted figures of dissected brain from [42] (with permission) showing some parts of (a) corticospinal tract, (b) superior longitudinal fasciculus, occipital fasciculus and uncinate fasciculus.

fibers connect the left and right side of the occipital lobe and they could be seen mostly in the central and most posterior white matter region in the corresponding axial slice of the brain. There are also other commissural fibers in brain which are relatively much more smaller than corpus callosum, such as the anterior commissure and posterior commissure which have very small sagittal cross section diameter 5 mm, but they start fanning and expanding towards the cortex of both hemispheres that interconnect much larger regions of the cortex.

Association fibers are groups of fibers which connect regions within the hemisphere. Some of the association fibers may be very long as they could run between the frontal and occipital lobes passing through the coronal sections of the brain. These long association fibers are termed fasciculi (fasciculus in singular form). Short association fibers connect adjacent cortex regions and they all are termed generally as short U-fibers. Long association fibers are named more specifically with their location and connecting cortex regions. The complexity of these fibers and their bending structure make the definition of the tract very difficult. Therefore the definitions might be rather course or similar. One such prominent fasciculus is the superior longitudinal fasciculus (SLF). It is located at the superior part of the hemisphere and these fibers run between different sites of the frontal, temporal, and parietal lobes that in

between some fibers deviate downward or forward from central part of this pathway and reach to the sites of the parietal and temporal lobes, and some fibers might reach up to the occipital lobe, as well. Therefore SLF has a broad anatomy. Another group of association fibers is named as inferior longitudinal fasciculus which connects the temporal and occipital lobes with a relatively linear pathway. There are also inferior and superior fronto-occipital fasciculus that could be coarsely defined as the pathways which connect visual nerves all the way to the occipital lobe and from the occipital lobe these fibers run forward back to the frontal lobe. One other main association pathway is cingulum which is covered with the cingulate gyrus and located within the limbic system. Cingulum is a very long bundle which runs above the corpus callosum winding around the genu and turning around the splenium, and ends in the hippocampal gyrus associating fibers of the hippocampus, amygdala and thalamus with prefrontal cortex.

Projection fibers are also a group of long fibers that unite the cortex with the lower parts of the brain such as thalamus, caudate nucleus, and putamen. Different projection fibers might unite in certain regions such as internal and external capsules, and cerebral peduncles. Coronal radiations also includes projections to the cortex with a shape of fanning structure towards the cortex. The fibers passing through these regions might also project to different parts of the brain such as cerebellum and spinal cord. The projection fibers run between the cortex and the spinal cord makes a known pathway called corticospinal tract. It passes through the coronal radiations, internal capsule, cerebral peduncles, and pons to reach its crossing region and go all the way down in the spinal cord to its controlling muscle or tissue.

In summary, axons of the neurons connecting distant sites are supported and covered by the myelinated fatty structure that makes the white matter brighter than the gray matter. These axonal fiber tracts carry impulses within a sophisticated sensory network that in the brain it has a complex but marvelously organized connectivity structure. The microscopic post mortem studies identified several short and long connections and according to its connecting regions they are classified in different groups. However since there are crossing and bending regions in which different fibers share the same anatomical region, the edges and the region limits of most of the classified

pathways are not certain and it is difficult to have complete understanding of the neuroanatomy of the white matter fibers. Knowing all these difficult issues, emerging in vivo brain imaging methods help to understand specific mechanisms of the brain that the imaging based attributes correlate up to a certain degree with the structural and functional neuroanatomy. The next section is about a gold standard imaging mechanism which is based on the diffusion contrast of the magnetic resonance imaging that could measure the fiber orientation distribution in white matter tissue. Following studies included novel algorithmic schemes to estimate neuroanatomical structure of the white matter that could show the characteristics of the neurodegenerative diseases.

2.2 The Brain Tractogram

The pathways of the axons in the brain constitute a sophisticated network which is nowadays called the brain connectome. This wiring structure is important in the functioning of the brain such that if there exists a deformation due to a disease or degeneration on a pathway, its controlling mechanisms might possibly be broken. In the previous section we introduced the white matter pathways mostly with ex vivo imaging methods that are important to learn neuroanatomy. On the other hand, in vivo imaging of the brain is important to characterise the diseases that it guides the treatment and helps to follow-up the progress.

Noninvasive imaging of the brain has been progressively improved by several key studies, as first, in quantum mechanical and magnetic properties of the substances such that Otto Stern, Isidor Isaac Rabi, and Walfgang Pauli were awarded the Nobel Prize in 1943, 1944, and 1945, respectively, for their contributions. After that, the concept of magnetic resonance imaging method became available with consecutive and impressive ideas of the scientists from different backgrounds, such as physics, chemistry, and medicine, that some of them were also awarded the Nobel Prize for their contributions. In 1952 the Nobel Prize of physics was shared by Felix Bloch and Edward Mills Purcell for their contribution to the magnetic resonance properties of certain solid and liquid substances. In 1954 Carr and Purcell explained in [43] simply that the diffusion

of water could be measured using a spin echo technique [44]. In that time, diffusion was actually a phenomenon which reduces the signal strength so that it needed to be eliminated. These studies were still at the spectroscopic domain. It took more than 30 years to get the first two dimensional images of a slice. First, in 1973, Paul Lauterbur considered generation of slight magnetic field gradients to reconstruct a slice of the specimen inside the magnet using projections [45]. This was a seminal study and it was followed by other developments such as frequency and phase encoding of the radio frequency pulses to locate received signals within the slice [46], [47]. Hence, magnetic resonance spectroscopy became a noninvasive and volumetric multi slice imaging method to characterize molecular constitutes of the human body including the brain. For their contributions, Paul Lauterbur and Peter Mansfield shared the Nobel Prize of Medicine in 2003.

Diffusion coefficient of the spins was first formulated in 1965 by using a pulsed gradient technique [48] with $S(TE) = S(0)exp(-bD)$, where D is the apparent diffusion coefficient (to be measured), b is the strength of the pulsed gradient, $S(0)$ is the signal intensity when the diffusion gradient strength vanished during the scan, and $S(TE)$ is the signal intensity at time of echo in the presence of strong diffusion gradients. Signal attenuation due to the diffusion of the spins was obtained in a form of an exponential decay. At that time, it is experimented for dry glycerol for which the diffusion coefficient was $(2.5 \pm 0.2) \times 10^{-8}$ cm^2 sec^{-1}, whereas for H_2O the diffusion coefficient was $(2.34 \pm 0.08) \times 10^{-5}$ cm^2 sec^{-1}. It was shown that the diffusion in dry glycerol is restricted within its medium. Approximately three decades later, Basser et. al. introduced using also off-diagonal pulsed gradients in a spin echo MR sequence such that the diffusion gradients are applied in at least 6 co-linear directions (XX,YY,ZZ,XY,XZ,YZ) [11]. Once the diffusion coefficients along the applied diffusion gradients are obtained, all these measurements $S(ij)$ could be employed offline in Eq. 2.1, from which the restricted diffusion characteristics of the medium is inferred with numerical solutions for the diffusion tensor D_{ij}.

$$ln[S(ij)/S(0)] = [-b_{ij}D_{ij}] \tag{2.1}$$

Diffusion tensor (D_{ij}) is a 3 by 3 symmetric matrix which could be diagonalized numerically and the shape of the diffusion ellipsoid could be inferred with the eigenvalues ($\boldsymbol{\lambda} = [\lambda_1 \geq \lambda_2 \geq \lambda_3]$) and corresponding eigenvectors ($\boldsymbol{v_1, v_2, v_3}$) [27]. Principal direction of the ellipsoid was expected to show the direction of the restricting microscopic walls in the medium. For the brain, restricted diffusion was observed in white matter regions and the principal direction was showing the directions of the white matter fibers. Diffusion tensor and its decomposition provided distinct microstructural characteristics which are rotationally invariant measures such as fractional anisotropy (FA) (Eq. 2.2), mean diffusivity (MD= $Trace(\boldsymbol{\lambda})/3$) or also called mean apparent diffusion coefficient (ADC) , axial diffusivity (AD= λ_1), and radial diffusivity (RD= $(\lambda_2+\lambda_3)/2$).

$$\text{FA} = \sqrt{\frac{3((\lambda_1 - \text{MD})^2 + (\lambda_2 - \text{MD})^2 + (\lambda_3 - \text{MD})^2)}{2(\lambda_1^2 + \lambda_2^2 + \lambda_3^2)}} \tag{2.2}$$

Although the diffusion tensor model has been very successful showing 3D structure of the brain white matter, it was assumed that the diffusion was Gaussian and it was not fully adequate to show the real microscopic structure of the brain which includes fiber crossings in many regions.

The developments to the diffusion MR sequences first included using more gradient orientations in addition to the off-diagonal pulsed gradients. Moreover, diffusion acquisitions with higher gradient strengths (high b value shells) have shown to contribute to the understanding of diffusion phenomenon in different tissue levels [49], [13], [50]. Development of new mathematical models such as multi tensor model [51], spherical harmonics representation [52] were followed to fit better to the shape of the measured diffusion orientation distribution function (ODF) with the emerging diffusion direc-

tional contrast and varying gradient strength.

An ensemble average propagator function is defined for the displacement of diffusing spins, in model-free (non-parametric) approach by integrating the measured diffusion signal along radial directions to form an ODF and it is computed by using Eq. 2.3 which integrates projections of diffusion signals, $P(r\mathbf{u})$, on each radial direction $\mathbf{u}$.

$$\Psi(\mathbf{u}) = \int_0^\infty P(r\mathbf{u})dr \tag{2.3}$$

Formulation of the diffusion model within spherical coordinates provided more comprehensive transforms of the diffusion signal. Some of the proposed transforms reputed to be model free such as spherical deconvolution method [53] and diffusion orientation transform method [54]. In general, model free methods aim to reconstruct a fiber orientation density function from which fiber directions could easily be obtained using peaks of the density function.

A way of analysing the ODF is to make use of spherical harmonic (SH) basis functions $Y_l^m(\mathbf{u})$, which is described clearly in [55]. Here l represents the order of the SH and $m \in \{-l, ..., 0, ..., l\}$ is an index for $2l + 1$ SH functions of order l.

Similar to the Fourier principle, a function defined on a sphere can be represented as a linear combination of SHs:

$$f(\theta, \varphi) = \sum_{l=0}^{\infty} \sum_{m=-l}^{l} c_{l,m} Y_{l,m}(\theta, \varphi) \tag{2.4}$$

Coefficients of each SH is given by:

$$c_{l,m} = \int_0^{2\pi} \int_0^{\pi} f(\theta, \varphi) Y_{l,m}^*(\theta, \varphi) sin\theta d\theta d\varphi \tag{2.5}$$

As depicted in Figure 2.4, we note that 0^{th} order SH series is an isotropic model forming a sphere, and 2^{nd} order SH series is identical to a diffusion tensor model having a single anisotropic SH. As higher order terms are included in series description we explore more complex underlying structure. 4^{th} order SH series expansion could resolve two fiber crossings and higher order terms represent mostly the noise in data acquisition.

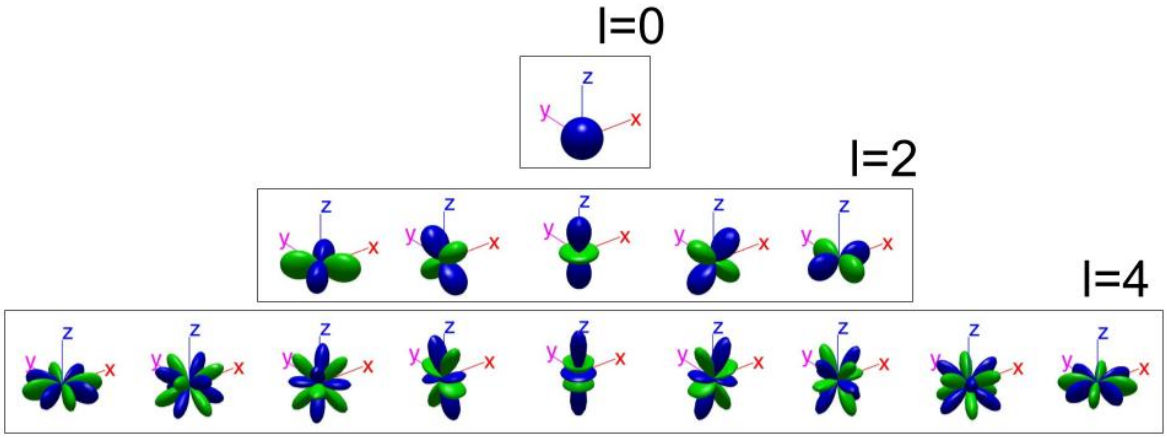

Figure 2.4 Visual representation of even order SH functions. Adopted from the internet [https://www.mathworks.com/matlabcentral].

Tourneir et. al. [53] proposed to model diffusion signal attenuation as a convolution of a sample response function in a peanut shape. A density function is estimated depicting the orientation distribution of the fibers, which is called fiber orientation density (FOD). FOD is obtained by the deconvolution of the measured signal attenuations with the sample response function. Probabilistic tractography schemes are then employed which samples most probable directions of FOD function to follow the streamlines [56]. Seeds are uniformly distributed on the brain to construct a tractogram. A typical tractogram might contain at least 100 thousand fibers.

Tractography algorithms mostly use a brain mask and predefined thresholds on FA and curvature to stop tracking. For a better tractogram these stopping criteria are not enough which is lack of anatomical information. Smith et. al. [15] consider implementing a new scheme to accept or reject tracked fiber by using anatomical constraints (segmented regions of brain: white matter, gray matter, CSF, and subthalamic regions).

Since tractogram seeds are uniformly distributed over the brain, the number of fibers passing through a voxel is biased and does not satisfy the underlying tissue density. To overcome this bias Smith et. al. [57] proposed a filtering scheme (called SIFT) to remove fibers from the tractogram so that a new form of a diffusion model, which could be reconstructed by using the contribution of the remaining fibers passing through a voxel, would resemble the measured diffusion. A tractogram is fed as an input to SIFT algorithm together with the FODs, and the output is a relatively less number of fibers that fit on the underlying diffusion model estimate. We could then drive unbiased track based statistics, such as average FA along the fibers passing through a voxel, to obtain track weighted images (contrasts) which could help to infer diagnosis of clinical cases [58].

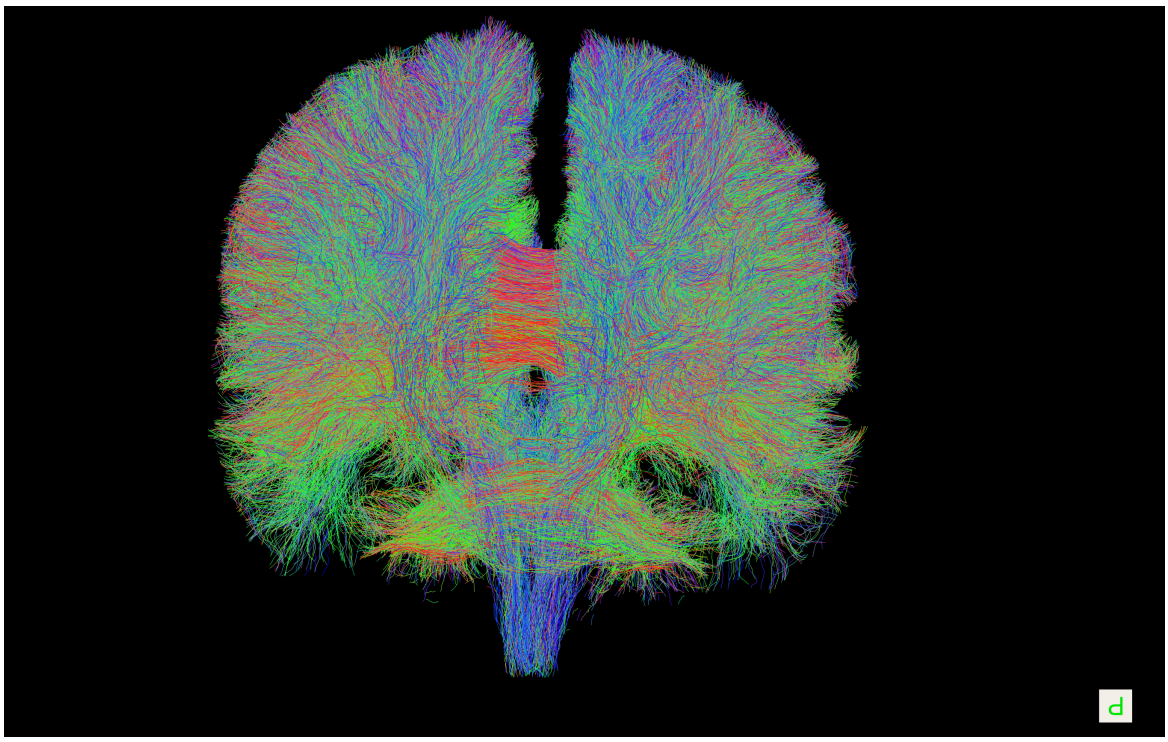

Figure 2.5 A tractogram of brain from our Schizophrenia dataset after SIFT.

3. METHODS AND VALIDATIONS

3.1 Dispersion of a Tract Profile

In this section, the dispersion of a set of fibers is defined mathematically to measure the shape variability at the macroscopic scale. We considered that each fiber is represented by a consecutive set of 3D points, and used endpoint statistics to quantify the dispersion. Definitions are exemplified using a tractogram of kissing fibers dataset, which is depicted in Figure 3.1(a). Fibers passing through a small sphere ($r = 1$ mm) (illustrated as dark blue color in Figure 3.1(b)) are truncated by another sphere ($R = 35$ mm) (depicted as red color (with a certain opacity value of 0.3) in Figure 3.1(b)). Hence, the points of each fiber, which are outside the region of this (truncation) sphere, are trimmed. In Figure 3.1(c), the intersection points of the truncation sphere and the fibers are depicted as green and red spheres on the surface of the truncation sphere.

Let a truncated fiber X_i be in the set of fibers $\{X_i : i \in \mathbb{N}\}$, and each fiber is represented as a set of 3D points such that $X_i := (x_{i,1}, x_{i,2}, ..., x_{i,n}, ..., x_{i,m})$ with point coordinates $x_{t,n} \in \mathbb{R}^3$, and m is the number of points on the truncated fiber.

Let $X^{(s)}$ and $X^{(e)}$ be a set of start and end points respectively of a truncated fiber which is in the set of fibers $\{X_i : i \in \mathbb{N}\}$, and $x_c^{(s)}$ and $x_c^{(e)}$ are centroids ($\in \mathbb{R}^3$) computed by averaging the 3D point coordinates in the sets $X^{(s)}$ and $X^{(e)}$. The sets of $X^{(s)}$ and $X^{(e)}$ initially contain only the first fiber's start and end points, which is like $X^{(s)} = \{x_{1,1}\}$ and $X^{(e)} = \{x_{1,m}\}$, and centroids of start and end points are assigned accordingly as $x_c^{(s)} = x_{1,1}$ and $x_c^{(e)} = x_{1,m}$. For the remaining fibers ($i = 2, 3, ..., m$) an iteration is started. Start and end points are added to $X^{(s)}$ and $X^{(e)}$ considering the closest alignment to the centroid of each set by comparing distance to the centroids, $x_c^{(s)}$ and $x_c^{(e)}$. if $x_{i,1}$ is closer to $x_c^{(s)}$ than $x_c^{(e)}$, then $x_{i,1}$ is added to $X^{(s)}$ and $x_{i,m}$ is added to $X^{(e)}$, i.e. $X^{(s)} = \{X^{(s)}, x_{i,1}\}$, and $x_{i,m}$ is added to $X^{(e)}$ by the same

way ($X^{(e)} = \{X^{(e)}, x_{i,m}\}$). Otherwise, end points are assigned to reverse sets such that $X^{(s)} = \{X^{(s)}, x_{i,m}\}$ and $X^{(e)} = \{X^{(e)}, x_{i,1}\}$. At the end of these iteration steps, centroids $x_c^{(s)}$ and $x_c^{(e)}$ are updated considering the recent addition to the sets $X^{(s)}$ and $X^{(e)}$, and a new iteration is started for the next fiber($i = i + 1$). This alignment produces a clustered representation of start and end points as depicted with green and red spheres in Figure 3.1(c).

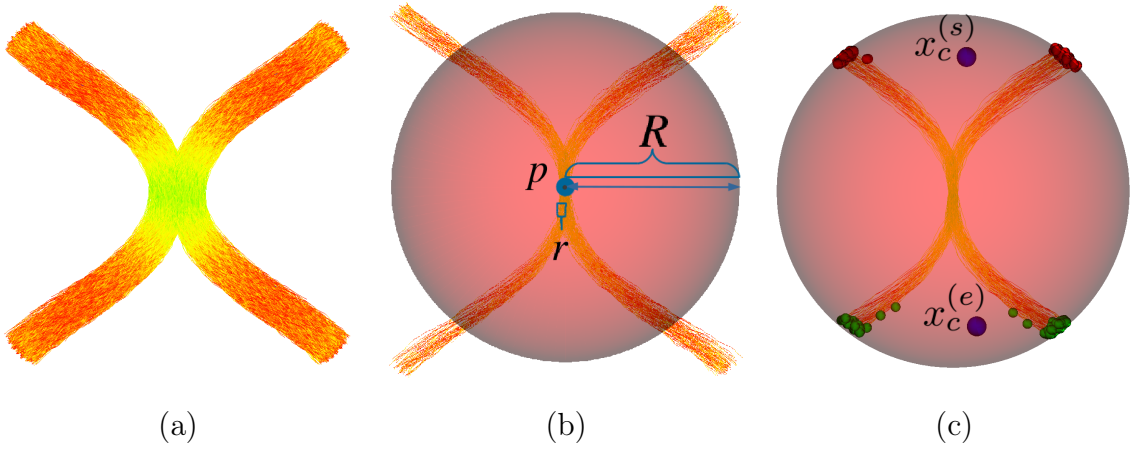

Figure 3.1 Kissing fibers dataset (a). Two spheres ($r = 1$ mm (blue) , $R = 35$ mm (red color with an opaque view)) both centered at the kissing point p (b). Start and end points (red and green spheres on truncation surface) of the truncated fibers (c).

We propose to use the variance of the clustered end points ($\sigma^{2(s)}$ and $\sigma^{2(e)}$) as a dispersion measure defined by Eq. (3.3) (the sum of the variances is normalized using the radius of truncation sphere, R):

$$\sigma^{2(s)} = \frac{1}{N}\sum_{i=1}^{N}(\|(X_i^{(s)} - x_c^{(s)}\|_2)^2 \tag{3.1}$$

$$\sigma^{2(e)} = \frac{1}{N}\sum_{i=1}^{N}(\|(X_i^{(e)} - x_c^{(e)}\|_2)^2 \tag{3.2}$$

$$\delta_p = \frac{1}{R^2}(\sigma^{2(s)} + \sigma^{2(e)}) \tag{3.3}$$

In Eq. (3.3), δ_p represents the estimated macroscopic dispersion measure for the center point in real coordinates, $p \in \mathbb{R}^3$, where ROI and truncation spheres are located (Figure 3.1(b)), and $x_c^{(s)}$ and $x_c^{(e)}$ are centroid points of the sets $\{X_i^{(s)}, i = 1, 2, ..., N\}$ and $\{X_i^{(e)}, i = 1, 2, ..., N\}$, respectively. This definition naturally forms a sampling scheme over the real coordinates. In theory, a dispersion map (Δ) is a mapping from $\mathbb{R}^3$ to $\mathbb{R}$, which could be sampled over a grid of volumetric image. The value of p can be set to any real coordinate within the image/tract boundaries and could be iterated for any image resolution so that different samplings of macroscopic dispersion maps are obtained. Given a tractogram and volume spacings (resolution), Δ is sampled by iterating the value of p for the real coordinate centers of each voxel by following the steps described above in this section (Section- 3.1) to form a unique dispersion map of the given tractogram.

Mathematically, dispersion value becomes 1.0 when there are two bundles exactly crossing at 90 degrees and each fiber in a bundle starts and ends at the same point, whereas the dispersion value becomes 0.0 when there is a single bundle that all the fibers start and end at the same point. In the case of fibers dispersing more than 90 degrees the dispersion value becomes more than 1.0.

Figure 3.2 depicts different samples of the proposed macroscopic dispersion measure on the crossing, kissing, and fanning synthetic bundles. Point p_1, sampled on the center of the crossing tractogram, has two totally dispersed endpoint sets that the computed dispersion measure, $\delta_{p_1} = 0.963$, is close to 1.0. At the edge of the crossing region dispersion is decreased drastically as depicted for p_2 and p_3, where dispersion values are $\delta_{p_2} = 0.463$, and $\delta_{p_3} = 0.003$. The point p_4 is sampled from the non-crossing region where the fibers coherently move towards the same direction so that computed dispersion value, $\delta_{p_4} = 0.004$, is very close to 0.0. On the other dataset, for the given

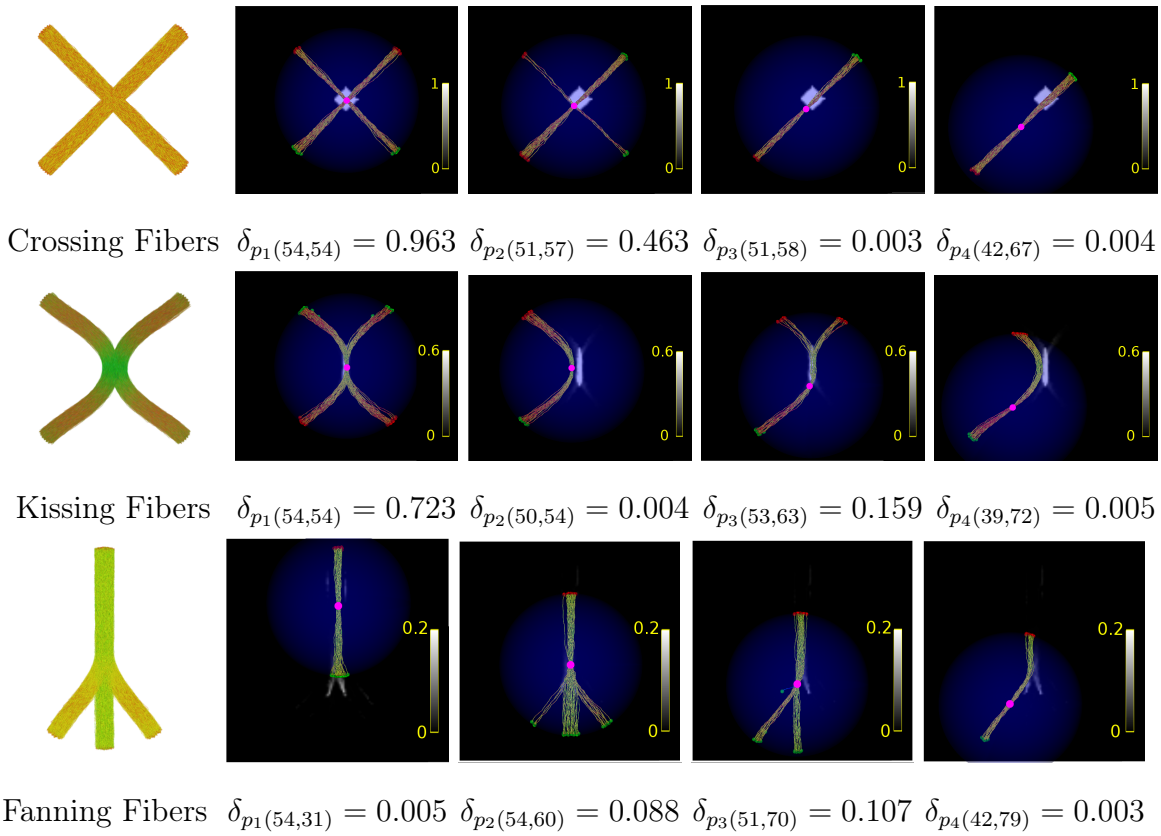

Figure 3.2 Selected points and their dispersion characteristics are given for crossing (1^{st} row) , kissing (2^{nd} row), and fanning (3^{rd} row) bundles in row-wise organization. Bundle tractograms are shown in left-most images, whereas the right-sided images depict first a background layer with the dispersion map of the tractogram. Second layer overlays a dot in pink color for the selected point, $p_i(column, row)$. The third layer contains the fibers passing through p_i, which are overlaid together with the truncation sphere in dark blue color, where $R = 35$ mm. A fourth layer contains the clustered end points of each fiber, which are shown as red and green small spheres. Dispersion values (δ_p) are given below for each p_i.

kissing bundles, there are four points that each possesses a different endpoint statistics (Figure 3.2 second row). At the center point, p_1, the dispersion ($\delta_{p_1} = 0.723$) is higher than the dispersion value computed for other points, whereas at a neighboring point p_2, the fibers coherently propagate and the dispersion value is $\delta_{p_2} = 0.004$. For the point p_3 on kissing bundles, at the lower surface of truncation sphere, end points are condensed within a small region, however, the fibers are separated after passing the kissing region, so that the end points at the upper surface become slightly dispersed, and the proposed method computes a higher dispersion ($\delta_{p_3} = 0.159$) compared to δ_{p_2}. The next point, p_4, is sampled on a coherent region that the fibers do not get dispersed ($\delta_{p_4} = 0.005$) but visit the neighboring voxels of the kissing region and keep moving coherently. Similar demonstrations are depicted in Figure 3.2 third row for the fanning

bundles dataset, such that the range of dispersion values are lower than the range of dispersion values in the kissing and the crossing bundles. For the fanning bundles dataset, p_1 is located at the superior and coherent region, and therefore, dispersion value is very small ($\delta_{p_1} = 0.005$), whereas p_2 is located at the upper neighbourhood of the intersection of fanning bundles that the fibers start fanning into three different directions, so that we compute an increased dispersion ($\delta_{p_1} = 0.088$) with respect to δ_{p_1}. As a next sample, p_3 is located in the intersection of two fanning bundles, where the fibers are coherent in one side but they get dispersed in the other direction, and dispersion value becomes slightly increased ($\delta_{p_3} = 0.107$). The last image depicts characteristics of the point p_4, which is closely located at the end of the fanned bundle, hence there is no intersection of different bundles, and the bundle is completely coherent ($\delta_{p_4} = 0.003$).

3.2 Synthetic datasets

We studied three different synthetic dMRI datasets. Kissing, crossing, and fanning bundles datasets, as shown in Figure 3.2, were generated using the Phantomas tool [59] in order to be used for validation studies. The isotropic resolution of synthetic images was 1.0 mm and the matrix size was 100 x 100 x 100, where diffusion-weighted images were generated in 32 directions.

3.3 Experiments and results on synthetic datasets

Experiments on synthetic datasets were designed to demonstrate characteristics of the proposed dispersion measure for the tuning parameter of R, which defines the macroscopic scale. We observed that the radius of sphere ROI, r, determines the degree of partial volume effects. Therefore, we fixed r according to the axial voxel spacings. We used heuristic parameters for the tractography and tractogram generation. Reconstructed tractograms were sampled over the diffusion space and a dispersion map was computed as described in Section-3.1.

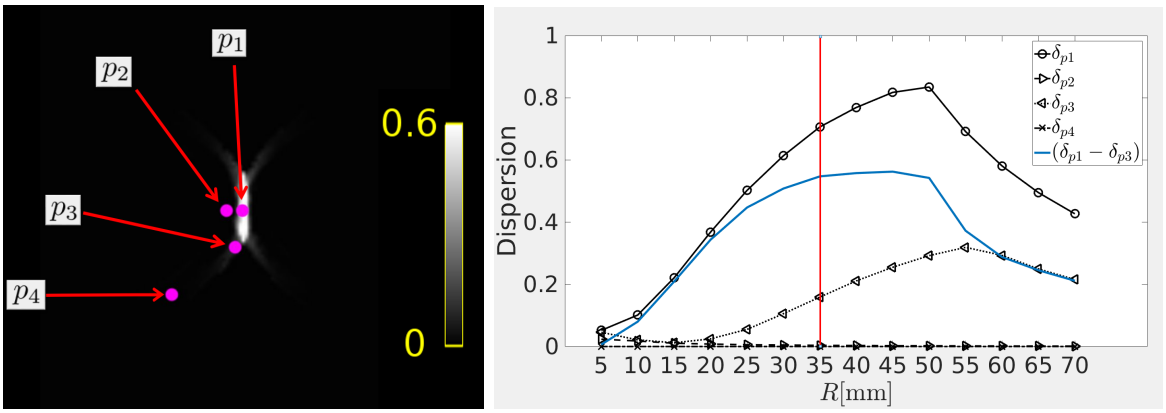

(a) (b)

Figure 3.3 Dispersion value (y-axis) versus different R values (x-axis) on kissing fibers dataset. Figure (a) displays four sample points (p_1, p_2, p_3, p_4) on dispersion map of kissing fibers dataset computed for $R = 35$, and (b) is the plot showing dispersion values of the picked four points for the range of $5 \leq R \leq 70$ mm (r is fixed to 0.5 mm).

In Figure 3.3(a), predefined points, p_1, p_2, p_3, and p_4, which were depicted separately in Figure 3.2 second row, were overlaid together, whereas in Figure 3.3(b), dispersion profiles of each point were plotted as a function of R. For this experiment, r was fixed to 0.5 mm and dispersion value of each point was computed for a range of R values between 5 mm and 70 mm. Point p_2 and p_4 were located on single bundle regions, therefore dispersion was independent of R and it was less than 0.05. However, we observed that dispersion characteristics of p_1 and p_3 changed with increasing R. Since p_1 was at the center and the fibers of p_1 were dispersed in both ends, with increasing R, dispersion is increased as the truncation sphere became bigger and end points became more dispersed until the end points reside inside the truncation sphere at $R = 50$ mm. For $R > 50$ mm, dispersion was decreased because the endpoint statistics remain the same but the normalization factor (R^2) caused a drastic decrease of δ_{p_1}. Dispersion plot of the point p_3, where the fibers were dispersed on one side but they were coherent on the other side, was similar to p_1, however, the dispersion value was not bigger than 0.25 and the maximum dispersion was observed for $R = 55$ mm. Specifically, we investigated the dispersion contrast of p_1 and p_3, i.e. formulated as $(\delta_{p_1} - \delta_{p_3})$, and plotted as a blue line, from which we observed that the contrast was not increased after a certain threshold of $R = 35$ mm. Since the mean bundle length of

this dataset was ~ 100 (± 5) mm, we heuristically observed a tuning of R that showed an optimum dispersion contrast of different regions by setting R as less than the half of the mean bundle length. Since the mean length of the fibers was approximately 60 mm for a sample real dataset, we chose R as 20 mm in real data experiments.

4. MACRO-STRUCTURAL DISPERSION CHANGES IN SCHIZOPHRENIA AND BIPOLAR DISORDER

4.1 Dataset

Previously published [60] real dMRI dataset has 52 normal, 49 schizophrenia, and 40 bipolar patients included in the processing framework. Diffusion scan was acquired using GE Medical Systems Signo 3T MR with the TR/TE of 14000/81.5, slice thickness of 2.5 mm, 256x256 image plane with equal x and y spacing of 0.9375, 8 channel head coil, single shell diffusion weighting with 5 consecutive $b = 0$ images and 31 directional sampling on the unit sphere with $b = 1000\ s/mm^2$.

4.2 Image preprocessing framework

We used MRtrix[1] software package for diffusion modeling and tractogram generation. We also used FMRIB Software Library (FSL) [61] for eddy current and motion correction, and Brain Extraction Tool (BET) [62] to create brain mask, and some FSL utility commands for the operations on intermediate image formatting. Registration steps were performed using FSL-FLIRT for linear registration followed by Diffeomorphic Demons Algorithm [63][2] for non-linear registration. For anatomically constrained tractography [64], T1 weighted high resolution ($0.9375 \times 0.9375 \times 1$ mm) image was registered linearly to diffusion space and segmented using 5tt segment command of MRtrix package in which we used FSL option.

Eddy current and motion corrected images were used both for response function estimation and Fiber Orientation Distribution (FOD) modeling of diffusion signal, and by using FODs a whole-brain tractogram having 1 million fibers were generated as an

[1] www.mrtrix.org

[2] Diffeomorphic Demons Algorithm is an option in Medinria tool, and source code is publicly available at http://hdl.handle.net/1926/510

output [64]. Before the computation of the dispersion map, the tractogram was filtered by an algorithm named as 'spherical deconvolution informed filtering of tractogram' (SIFT) [57] and 150 thousand of fibers remained after filtering, which computationally ensures that the remaining fibers after filtering best fit with the underlying FOD signal. All the diffusion preprocessing and tractogram generation operations were performed using the MRtrix package.

ICBM-DTI-81 white-matter (JHU) atlas [65] which has 48 WM tract labels and Juelich brain atlas [10] which has 10 WM regions on MNI152 space were used to determine group differences. The dispersion map was computed on the diffusion space. First, structural T1 image was used to register (linear and non-linear warp) subject space onto MNI. Second, the mean b0 image was registered onto the structural T1 image. Then, these two transformations were used to transform the dispersion map onto the atlas space.

4.3 Results

By following the diffusion image processing framework as described in Section 4.2, a tractogram of the brain was computed and later used to compute the dispersion map as described in Section 3.1, by setting the r (radius of sphere ROI) value to 1 mm, whereas the radius of the truncation sphere, R, was fixed to 20 mm. Experiments on real dMRI included a qualitative evaluation section that compares the dispersion to FA and mean b0 images, and that depicts the dispersion profiles for corresponding voxels of certain WM regions from BP and normal subjects that the proposed dispersion measure was increased or decreased in the BP group. Then, a statistical evaluation section is included for detailed group comparisons that were performed considering WM regions of both JHU and Juelich brain atlas.

Qualitative Evaluation

In Figure 4.1, the dispersion map of a normal subject within our dataset was compared to the FA and the mean b0 images of the same subject displaying axial slices that include corpus callosum and cingulum bundles. Dispersion map was overlaid on the mean b0 image such that if there was no fiber passing through the voxel, the dispersion value was null and the voxel depicted with the mean b0 contrast. As it can be seen from this figure, the dispersion was close to zero if the bundle was coherently moving towards two sides, e.g. the cingulum, and the genu and the splenium of the corpus callosum, whereas the dispersion was increased and became closer to 1.0 at the voxels for which the bundles were crossing or kissing, as observed in Figure 4.1 bright-yellow regions. The given slices in Figure 4.1(a) and (b) also included axial sections of some U-fibers for which the middle segment observed to have increased dispersion contrast having a bright-yellow intensity because this segment had a tight (kissing) contact with other bundles, however, this contrast was not observed in FA or mean b0 images.

We made the proposed framework available as a downloadable tool[3] , that could be used to compute and save dispersion map of a given tractogram file, and we displayed sample screenshots from the tool in Figure 4.2 for sample subjects from the BP and the normal group that the mean dispersion of the right cingulum and the right superior occipito-frontal fascicle were measured close to the group averages. For this experiment, we sampled a voxel whose anatomical label is known on the MNI space and transformed the voxel onto the subject space using the inverse linear and nonlinear registration steps obtained in the proposed registration framework. Hence, sampled dispersion profiles of each subject were coregistered and observations were sampled from the same WM region. What we observed was the difference between the groups, which was depicted using 3D fiber profiles of the corresponding anatomy. For the marked cingulum voxel of the BP subject, fibers became more dispersed having more dispersed fiber end points, in contrast, for the superior occipito-frontal fascicle voxel of the BP subject, fibers were not as dispersed as for the normal subject.

[3]https://bitbucket.org/_ali_demir/

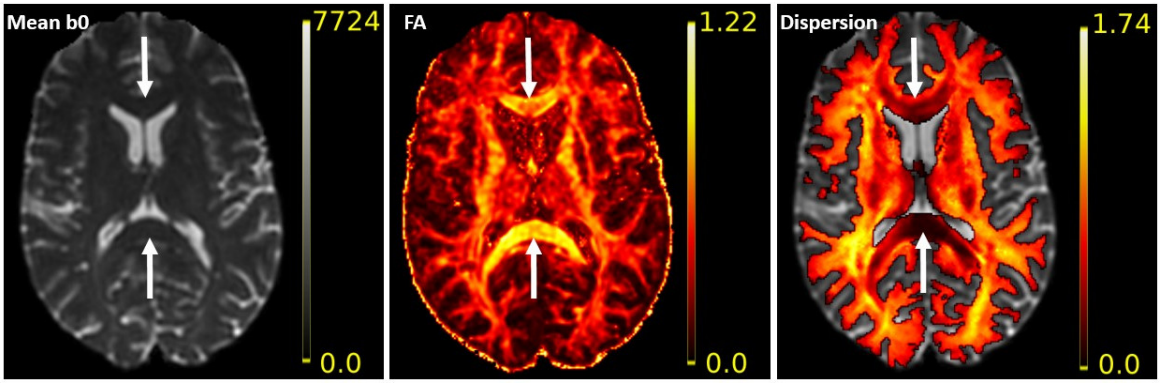

(a) Genu and splenium of corpus callosum

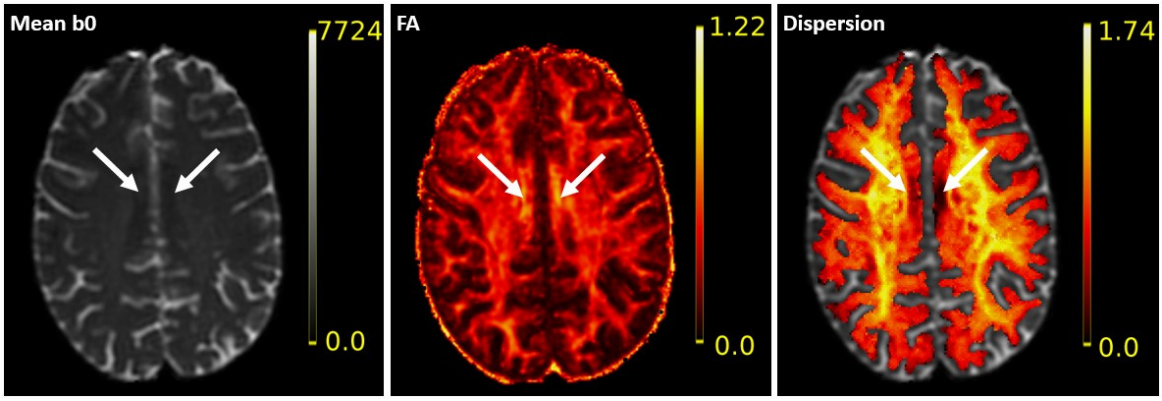

(b) Right and left cingulum

Figure 4.1 A comparison of mean b0, FA, and dispersion on corpus callosum and cingulum bundles. The dispersion map was overlaid on the mean b0 image. Figure (a) marked anterior edge of the genu of the corpus callosum with a downward arrow at the top of the image and posterior edge of the splenium of the corpus callosum with an upward arrow at the bottom of the image. Figure (b) marked the outer edges of the (radiological) right and the left cingulum with the arrows.

Statistical evaluation

We compared proposed macroscopic dispersion with local DAIs, such as fractional anisotropy (FA), apparent diffusion coefficient (ADC), radial diffusivity (RD), and axial diffusivity (AD). Proposed dispersion map was reconstructed by setting the r (radius of sphere ROI) value to 1 mm, whereas the radius of the truncation sphere, R, is fixed to 20 mm (considering our proposition that it should be less than the half-mean length of fibers, e.i., we choose R, such that $R \leqslant 30$ mm).

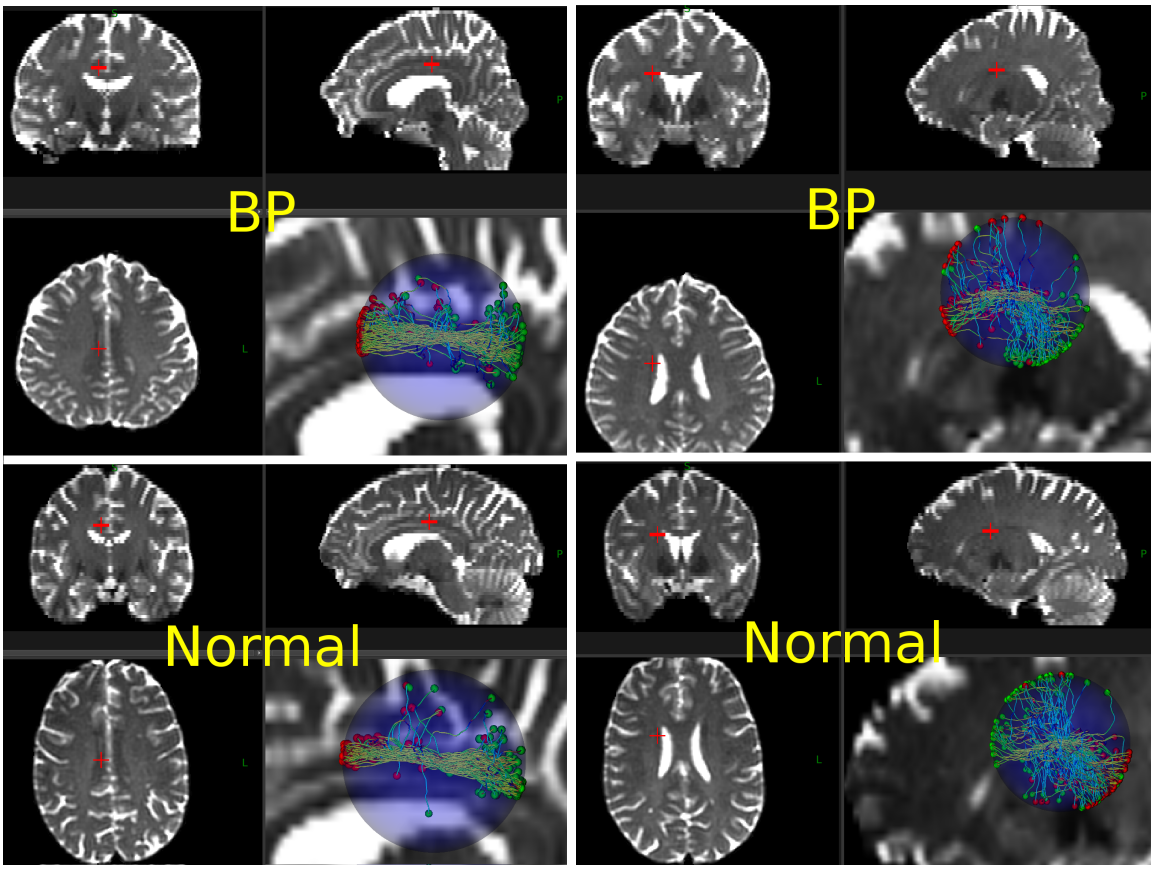

(a) (b)

Figure 4.2 A comparison of the dispersion on the right cingulum (a) and the right superior occipito-frontal fascicle (b), depicting 3D fiber profiles (on the right and bottom side of orthographic views) of corresponding (registered) voxels (marked with a cross sign in red color on the axial, sagittal, and coronal mean b0 images) of BP and HC subjects, where the dispersion of the marked voxel in (a) was computed as 0.65 for the BP subject and 0.45 for the normal subject, whereas in (b) dispersion was computed as 0.95 for the BP subject and 1.15 for the normal subject.

Statistical analysis was performed using DAI and dispersion maps which were registered to the MNI space as described in Section-4.2. Juelich and JHU atlases are two different maps of the brain in MNI space that the anatomical name of each brain voxel is known. We considered labeled WM structures (excluding gray matter) from Juelich and JHU atlases. We excluded certain WM regions, such as cerebellar peduncles, uncinate fasciculus, fornix, and acoustic radiation, due to their small volume and possible partial volume artifacts so that we focused on the greater WM structures, such as corpus callosum, cingulum, and long WM fasciculus as listed in Table 4.1 and Table 4.2.

Table 4.1
Statistical significance scores (p-values) of the group comparisons on WM labels of Juelich brain atlas.

	HC vs SCH					HC vs BP					SCH vs BP				
	FA	**ADC**	**RD**	**AD**	**Dispersion**	**FA**	**ADC**	**RD**	**AD**	**Dispersion**	**FA**	**ADC**	**RD**	**AD**	**Dispersion**
CB	0.0122	0.0041	0.0052	0.0333		0.0396	0.0071	0.0099	0.0114	**0.0007**					**0.0004**
Cingulum R					0.0062					**0.0003**					
Cingulum L										**<0.0001**					0.0055
CST R				0.0252			0.0113	0.0106		0.0079					0.0071
CST L				0.0141			0.0034	0.0498	**0.0019**	0.0198					0.0082
IOFF R						**0.0001**	**<0.0001**	**<0.0001**		**0.0009**	0.0050	0.0040	**0.0018**		0.0126
IOFF L							0.0369			**0.0002**					0.0062
OR R		0.0392		0.0311		0.0139		0.0213		**0.0025**				0.0388	0.0378
OR L		0.0142	0.0290	0.0086						0.0300		0.0371	0.0409	0.0435	0.0078
SLF R		**0.0005**	0.0342	0.0032	0.0354							0.0046		**0.0003**	
SLF L		0.0469		0.0221		0.0246		0.0494			0.0052			**0.0009**	
SOFF R										**0.0006**					0.0041
SOFF L				0.0440						**0.0006**					**0.0005**

Bonferroni corrected significant p-values ($p < 0.0029$) are highlighted by using boldface font, whereas p-values, which are greater than the corrected threshold but less than 0.05, are mentioned just for an insight. Non-significant p-values are not given. CB: Callosal body, CST: Corticospinal tract, IOFF: Inferior occipito-frontal fascicle, OR: Optic radiation, SLF: Superior longitudinal fascicle, and SOFF: Superior occipito-frontal fascicle. R and L are abbreviations for the radiological right and left side of the given tract respectively.

Juelich and JHU atlases are different in terms of their reconstruction method that the Juelich atlas is based on histological cuts of a post-mortem brain, whereas the JHU atlas is an atlas reconstructed by using labeled WM fibers which are reconstructed from dMRI data. Therefore, anatomical labels and label volume sizes are comparable such that even if the labels have the same name, they might not completely overlap in MNI space. For example, the corticospinal tract is named the same in both atlases but they do not completely overlap. In fact, corticospinal tract defined in Juelich atlas overlaps with parts of corona radiata and internal capsule defined in JHU, whereas corticospinal tract defined in JHU atlas is located in the brainstem that its superior label is internal capsule, which is followed by corona radiata. Superior longitudinal fasciculus also named the same in both atlases that in Juelich atlas the size of the tract is smaller than the tract defined in JHU atlas, and only central part of the tract is labeled in Juelich atlas, whereas in JHU atlas, the tract is defined including fiber ends connecting to the gray matter surface. Another example is the corpus callosum, which is labeled as a whole in Juelich atlas whereas in JHU, it is divided into three regions as the genu, the body, and the splenium of corpus callosum. Cingulum (cingulate gyrus) is the only bundle that has a similar size and shape in both atlases, and their regions mostly overlap, except that in JHU, cingulum has two different divisions: cingulate gyrus and hippocampus, such that the cingulate gyrus part is the superior part of the cingulum that it lies between the frontal lobe and the temporal lobe of brain whereas the hippocampus part starts from the temporal region of the brain and reaches to the hippocampus that this part is not defined in Juelich atlas. Because of the aforementioned differences between these two atlases, we considered WM regions from both atlases separately and we presented the statistical results respectively in different tables and figures.

Statistical significance tests were performed on each map, which were registered onto the MNI space. In these tests we compared mean values of the given measure over each atlas region for the healthy controls (HC), schizophrenia (SCH) and bipolar (BP) patients. First the one-way ANOVA method was used considering the mean values of the aforementioned measures including the proposed macroscopic dispersion measure. Then, post-hoc tests were performed only for the significant inter group differences.

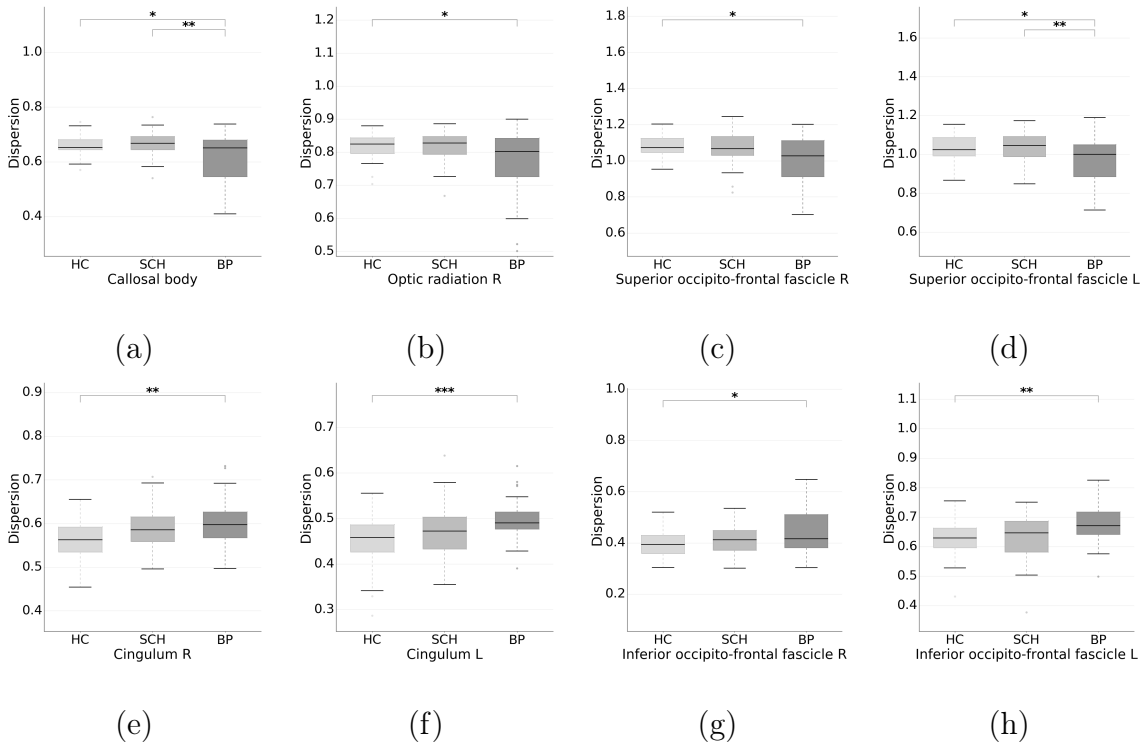

Figure 4.3 Whisker-Box plots comparing means of the dispersion measure between the healthy controls (HC), schizophrenia (SCH), and bipolar (BP) group that the difference between the groups is statistically significant for the given WM region of Juelich atlas. Bonferroni corrected statistical significance score is depicted using stars where * means $p < 0.0029$, ** means $p < 0.0006$, and *** means $p < 0.00006$. We exclude whisker-box plots of WM regions for which the difference between the groups is not significant ($p > 0.0029$).

In fact, there was at least one significant difference in most of the considered atlas regions, so that ANOVA test discards only certain JHU atlas regions. Posterior part of the internal capsule, anterior part of corona radiata, and thalamic radiation were the regions for which the difference between groups was not statistically significant. For each post-hoc analysis, that the atlas region is given, measured mean values of each group was first tested for normality and if both groups were normally distributed we used unpaired t-test, otherwise we used Mann-Whitney rank-sum test to obtain a significance score (p-value) of the compared groups. Since we performed multiple comparisons we used Bonferroni corrected p-value threshold (0.05 divided by the number of atlas regions) to label the comparison that the given atlas region possesses a significant discrimination for the disease. Significant atlas regions were given in Table 4.1 and Table 4.2 such that the significant p-values were highlighted by using boldface font and non-significant p-values were leaved empty, whereas p-values which were greater

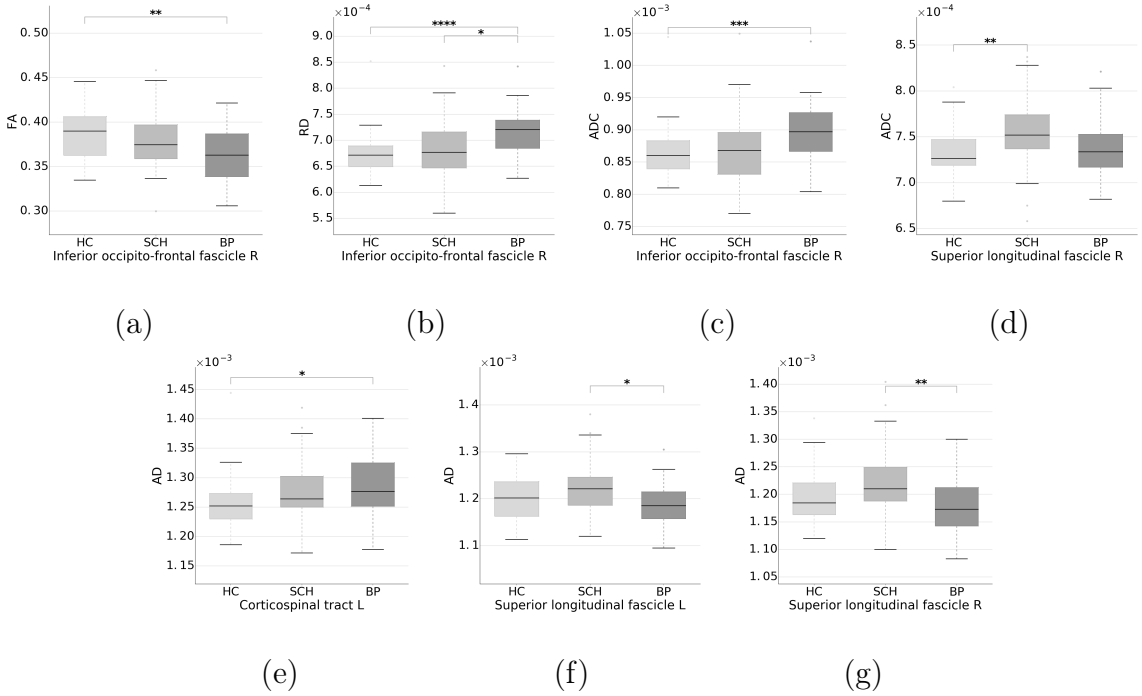

Figure 4.4 Whisker-Box plots comparing means of the DAI measures (FA, RD, AD, and ADC) between the healthy control (HC), the schizophrenia (SCH), and the bipolar (BP) group that the difference between the groups is statistically significant for the given WM region of Juelich atlas. Bonferroni corrected statistical significance score is depicted using stars where * means $p < 0.0029$, ** means $p < 0.0006$, *** means $p < 0.00006$, and **** means $p < 0.000006$. We exclude whisker-box plots of WM regions for which the difference between the groups is not significant ($p > 0.0029$).

than the corrected threshold and less than 0.05 was mentioned in the tables just for an insight.

Given the Table 4.1 and Figure 4.3, the proposed dispersion measure was found to be a candidate descriptive feature for comparing the bipolar and the control group considering most of the Juelich atlas regions. Compared to the healthy controls, it was observed that the dispersion value was decreased in bipolar group for the collosal body, the right optic radiation, and the right and the left superior occipito-frontal fascicle, as depicted in figures 4.3(a), 4.3(b), 4.3(c), and 4.3(d) respectively, whereas the bipolar group had significantly increased dispersion in both hemispheres of the cingulum and the inferior occipito-frontal fascicle, as depicted in figures 4.3(e), 4.3(f), 4.3(g), and 4.3(h) respectively. Comparing the differences between schizophrenia and bipolar group, for the proposed dispersion measure there was a significant decrease in the region of the callosal body, and the left superior occipito-frontal fascicle (figures

4.3(a) and 4.3(d)). Furthermore, we also observed in Figure 4.3 that none of the Juelich atlas regions were sensitive to the changes in the proposed dispersion measure for discrimination of the healthy control and the schizophrenia groups. However, statistical test score of the right cingulum comparing schizophrenia and control group was (given in Table 4.1 as 0.0062) at the boundary of Bonferroni corrected threshold that there was an insight of an increase in dispersion, which was shown Figure 4.3(e).

In terms of DAI measures, significance scores between the groups were given in Table 4.1 for the given Juelich atlas regions. For the right inferior occipito-frontal fascicle, bipolar group had significantly decreased FA and significantly increased RD and ADC compared to the healthy controls. We, here, mention again that the change in the dispersion measure was also found to be significant in both the right and the left inferior occipito-frontal fascicle. The only significant region, comparing schizophrenia and healthy control groups, was the right superior longitudinal fascicle that significantly increased ADC ($p = 0.0005$) was observed.

Increased AD in the left corticospinal tract in the bipolar group compared to the healthy control group was found to be significant ($p = 0.0019$). Comparing the bipolar with the schizophrenia group, we observed significantly decreased AD in both the left ($p = 0.0003$) and the right ($p = 0.0009$) superior longitudinal fasciculus, and a significantly increased RD in the right inferior occipito-frontal fascicle ($p < 0.0001$) as well. We also reported a slightly increased AD in the schizophrenia group compared to the healthy controls for both sides of superior longitudinal fasciculus that p-values were 0.0032 and 0.0221 respectively for the left and the right side, though the difference was not significant considering the Bonferroni corrected threshold.

As we have described the statistical comparison results of the diagnostic groups for the Juelich atlas regions, similar experiments followed considering JHU atlas regions as well. Statistical results from the JHU atlas regions were given in Table 4.2. In Figure 4.5, Whisker-box plots of the proposed macroscopic dispersion were depicted for the given region that the change is found to be significant, whereas we only stated the change of significant DAI measures for the selected regions.

The corpus callosum was labelled separately as genu, body, and splenium in the JHU atlas. In Figure 4.5(a) and (b), whisker-box plots show that there was a decreased dispersion in the body and the splenium of corpus callosum for the bipolar group compared to the healthy controls. We here mention again that the change in dispersion measure over the callosal body defined on Juelich atlas was also significant for the bipolar and the healthy control group comparison noting that the callosal body in Juelich atlas covers also the genu and the splenium. Since, the statistics of the dispersion obtained for schizophrenia and healthy control groups were similar in Figure 4.5(a), and the change was statistically non-significant, there was also a statistically significant decrease in the dispersion measured over the body of corpus callosum for the bipolar group compared to the schizophrenia group. Considering Figure 4.3(a) together with Figure 4.5(a) and (b), statistical significance pattern of Figure 4.3(a) was similar to the Figure 4.5(a) which indicates decreased dispersion was observed for the callosal body, however this could not be generalized for the genu of corpus callosum for which the change in dispersion was not significant.

Table 4.2
Statistical significance scores (p-values) of the group comparisons on WM labels of JHU brain atlas.

	HC vs SCH					HC vs BP					SCH vs BP				
	FA	ADC	RD	AD	Dispersion	FA	ADC	RD	AD	Dispersion	FA	ADC	RD	AD	Dispersion
Genu of CC					0.0405		0.0031	0.0052	0.0211			0.0126	0.0068	0.0435	0.0471
Body of CC	0.0227	0.0050	0.0035				**<0.0001**	**<0.0001**	**0.0002**	**0.0005**		0.0301		0.0057	**0.0001**
Splenium of CC		0.0283	0.0254	0.0375		0.0178	**0.0003**	**0.0007**	0.0073	**0.0010**					0.0040
CST R										**0.0003**				0.0243	**0.0006**
CST L										**0.0003**					**0.0004**
Ant. IC R										0.0054					
Ant. IC L		0.0419	0.0306			0.0255		0.0372		0.0403					
Retr. IC R		0.0466				**0.0004**		0.0026			0.0056			0.0045	
Retr. IC L		0.0137		0.0100		**0.0010**		0.0023	0.0433		0.0029			**0.0004**	
Superior CR R										0.0044					0.0323
Superior CR L		0.0206		0.0118						**0.0007**					0.0063
Posterior CR R	0.0351	**0.0003**	**0.0004**	0.0264						0.0055		0.0446			
Posterior CR L		0.0469								0.0248					
Sagittal Stratum R		**0.0008**	0.0100	0.0117								0.0395		0.0075	
Sagittal Stratum L		0.0044	0.0149	0.0306										0.0232	
EC R					0.0116					**<0.0001**					
EC L		0.0131		0.0168	0.0133		0.0082	0.0291		**0.0001**					0.0281
Cingulum R					**0.0016**					**<0.0001**					0.0472
Cingulum L										**<0.0001**					0.0027
SLF R		0.0136								**0.0012**		0.0200		**0.0003**	
SLF L					0.0288					0.0071				0.0431	
SFOF R										0.0142					
SFOF L										0.0023					**0.0013**

Bonferroni corrected significant p-values ($p < 0.0016$) are highlighted by using boldface font, whereas p-values, which are greater than the corrected threshold but less than 0.05, are mentioned just for an insight. Non-significant p-values are not given. CC: Corpus callosum, CST: Corticospinal tract, Ant. IC: Anterior limb of internal capsule, Retr. IC: Retrolenticular part of internal capsule, CR: Corona radiata, EC: External capsule, SLF: Superior longitudinal fasciculus, SFOF: Superior fronto-occipital fasciculus. Cingulum is the part of cingulate gyrus. R and L are abbreviations for the radiological right and left side of the given tract respectively.

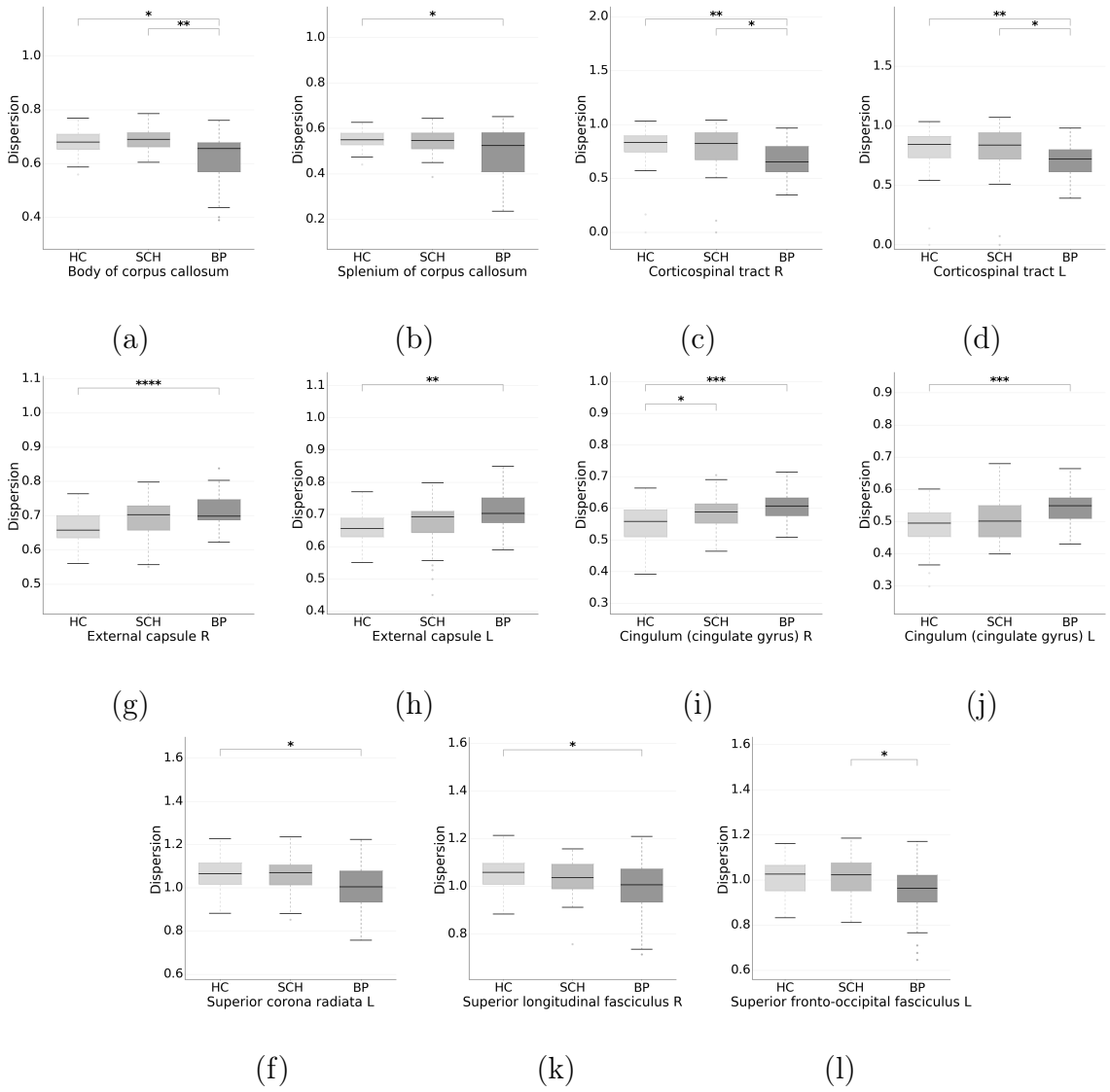

Figure 4.5 Whisker-Box plots comparing means of dispersion measure for different WM regions from JHU atlas between healthy controls (HC), schizophrenia (SCH), and bipolar (BP) group. Bonferroni corrected statistical significance score is depicted using stars where * means $p < 0.0016$, ** means $p < 0.0003$, *** means $p < 0.00003$, and **** means $p < 0.000003$. We exclude whisker-box plots of WM regions for which the difference between the groups is not significant ($p > 0.0016$).

Unlike the Juelich atlas, in JHU, the corticospinal tract is labeled as the region not being beyond the brainstem. Therefore the statistical results were different for each atlas. The dispersion statistics of the corticospinal tract were depicted in Figure 4.5(c) and (d) for the right and the left side respectively, where there was a significant decrease for both sides comparing the bipolar group with the healthy controls. Since the change in dispersion was not significant to differentiate the schizophrenia and the healthy control groups, there exists a distinction in dispersion measure for the bipolar

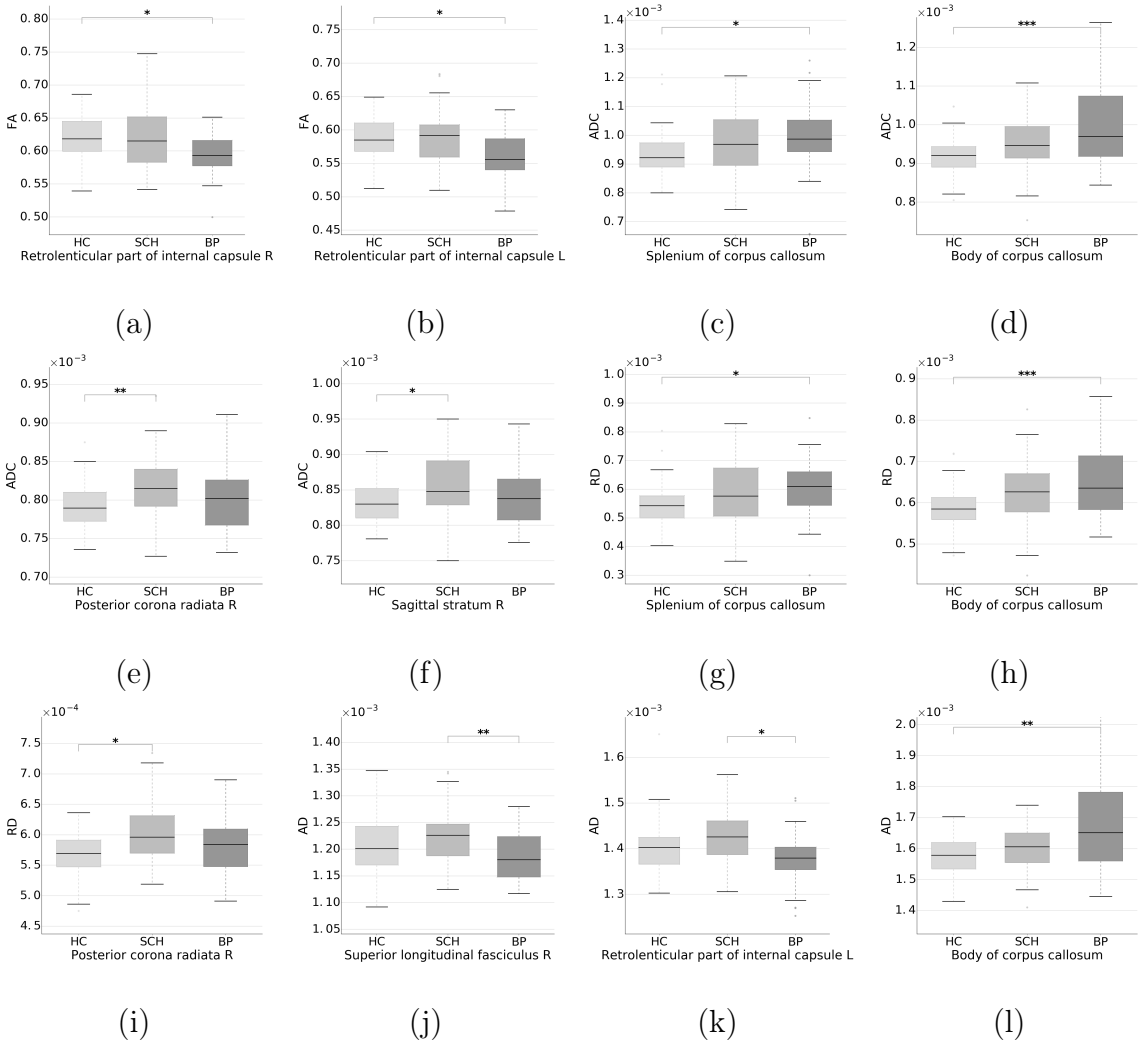

Figure 4.6 Whisker-Box plots comparing means of DAI measures (FA, RD, AD, and ADC) for different WM regions from JHU atlas between healthy controls (HC), schizophrenia (SCH), and bipolar (BP) group. Bonferroni corrected statistical significance score is depicted using stars where * means $p < 0.0016$, ** means $p < 0.0003$, and *** means $p < 0.00003$. We exclude whisker-box plots of WM regions for which the difference between the groups is not significant ($p > 0.0016$).

and the schizophrenia group comparison that dispersion was decreased significantly ($p < 0.0016$) for the bipolar group compared also to the schizophrenia group.

The external capsule defined in JHU atlas partially overlaps with the inferior occipito-frontal fascicle defined in Juelich atlas. As it might be expected, comparing the Figure 4.3(g-h) and the Figure 4.5(g-h), we observed similar changes in the dispersion for the external capsule and the inferior occipito-frontal fascicle that, independent of lateralization, there was a significant increase in the dispersion for the bipolar group compared to the healthy control group, whereas the change in dispersion was not

significant for the schizophrenia-healthy control and the bipolar-schizophrenia group comparisons.

Cingulate gyrus is the gray matter region from which the cingulum bundle projects, so that the bundle overlies the corpus callosum [66]. In JHU, cingulate gyrus part of the cingulum is separated from the hippocampus part of the cingulum, where the cingulate gyrus part mostly overlaps with the cingulum defined in Juelich atlas, and the statistical results were similar for both atlas regions as depicted in Figure 4.3(e-f) and Figure 4.5(i-j). Therefore, we reproduced that increased dispersion was observed in the cingulum (cingulate gyrus) defined in JHU atlas, for the bipolar group compared to the healthy control group. Here, in Figure 4.5(i), we also observed significantly increased dispersion ($p = 0.0016$) comparing the schizophrenia group with the healthy control group in the right cingulum, for which the significance test score of the increased dispersion in the right cingulum defined in Juelich atlas was 0.0062 for the schizophrenia-healthy control group comparison, which was given in Table 4.1 and depicted in Figure 4.3(e).

Besides, considering the proposed dispersion measure, a slight but significant decrease was observed in the left superior corona radiata and the right superior longitudinal fascicle comparing the bipolar group to the healthy controls as depicted in Figure 4.5(f-k). In addition, we reported in the Table 4.2 that the statistical test score for the change of the dispersion in the right superior corona radiata and the left superior longitudinal fasciculus were 0.0044 and 0.0071 respectively, which are very close to the Bonferroni corrected threshold of 0.0016 selected for JHU experiment. Therefore, it could be inferred that the decrease of the dispersion in the superior corona radiata and the superior longitudinal fasciculus might be independent of the lateralization. There was also a significant decrease in the left superior fronto-occipital fasciculus ($p = 0.0013$) comparing the bipolar group to the schizophrenia group, noting for the same tract that the decrease of dispersion for the bipolar group compared to the healthy controls might also be significant considering the obtained test score of 0.0023.

Statistical test results of the change in DAI measures were reported as the p-values in Table 4.2. For the right and the left retrolentucilar part of the internal capsule, there was a significant decrease in FA comparing the bipolar group to the healthy controls, where the p-values were 0.0004 and 0.0010 respectively. We also note from Table 4.2 that there was also an insight of a similar difference in FA considering the comparison of the bipolar and the schizophrenia groups that statistical test scores were 0.0056 and 0.0029 for the left and the right side respectively.

Compared to the healthy control group, an increased ADC for the bipolar group was observed in the body and the splenium of the corpus callosum such that the significance test scores were $p < 0.0003$ and $p = 0.0001$ respectively. Considering the ADC measure and schizophrenia-healthy control group comparison, we observed significant change for two different JHU atlas regions, the right posterior corona radiata ($p = 0.0003$) and the right sagittal stratum ($p = 0.0008$), that there was a significant increase. As for ADC, an increased RD was observed in the body and splenium of the corpus callosum ($p < 0.0001$ and $p = 0.0007$) for the comparison of the bipolar group with the healthy control group. As there was an increased ADC in the right posterior corona radiata for the schizophrenia group compared to the healthy controls, RD value in this region was also increased significantly ($p = 0.0004$) for the same comparison. Hence, we observed another similar change pattern for ADC and RD measures in the right posterior corona radiata for the schizophrenia-healthy control group comparison. In the right superior longitudinal fasciculus and the left retrolenticular part of internal capsule, only the difference between the bipolar and the schizophrenia group was found to be significant for AD measure (p values are $p = 0.0003$ and $p = 0.0004$ respectively), where there was a decreased AD in bipolar group.

We note that, considering the superior longitudinal fascicle defined in Juelich atlas, AD was decreased in both the left and the right sides. AD measure was also found to be significant for the bipolar-healthy control group comparison in the body of corpus callosum, such that there was an increased AD ($p = 0.0002$) in bipolar group. We also note that, AD, RD and ADC measures were both increased in the body of corpus callosum for the bipolar-healthy control group comparison.

4.4 Discussions

We proposed a method to generate a novel 3D map of a macroscopic feature of the brain that the intensity of each voxel in the proposed map is a cumulative information showing the degree of the deviation of WM structure far beyond the voxel. We also hypothesized that there might be WM regions such that the dispersion map of the region is useful to discriminate disease groups from the healthy controls.

It is known that the structural brain connectome is produced together with false positive connections [67]. However, at macro scales, the effect of weak connections found to be inconsequential as for the graph theoretical analysis [68]. Therefore, the tractogram is an important information source to be used as an input for the structural analysis of the brain. The proposed method intentionally considers the tractogram as an input and reconstructs a 3D map of the brain such that the proposed macroscopic dispersion is increased as the voxel locally having an increased fiber complexity so that the tracked fibers elongate from the local region into different directions and get dispersed at macro scales. One of the major strengths of the proposed method is that the macroscopic dispersion measure is also capable of detecting macroscopic characteristics of kissing fibers for which the fibers while locally coherent disperse gradually at macro scales.

Based on the previous dMRI studies on psychiatric disorders, structural abnormalities are identified frequently with reduced FA, and increased RD and AD in frontal and frontal associative brain WM regions such as cingulum, inferior occipito-frontal fasciculus and corpus callosum [69].

Consistent with the proposed hypothesis, we examined in the real dMRI experiments that macroscopic dispersion is also informative, together with the local dMRI measures, to distinguish disease groups, especially for the delineation of bipolar subjects and healthy controls. The implication for our findings is that greater dispersion obtained in cingulum and inferior occipito-frontal fasciculus might reflect an increased connectivity in the frontal or frontally associative brain WM regions, which is also

agreed with previous schizophrenia and bipolar studies that report increased activity in dorsolateral and prefrontal cortex [70], [71], [72]. Our data confirm a statistically significant relationship between increased dispersion measure and schizophrenia only in the right cingulum. For the bipolar disease, our findings report increased dispersion in cingulum and inferior occipito-frontal fasciculus, which implicated an increased connectivity, however there is a decreased dispersion in corpus callosum and superior occipito-frontal fasciculus that a decreased connectivity is thought to be implicated for these regions. We here cite a microsurgical study of Türe et. al. [73] that they proposed the fiber fasciculus of the occipital lobe do not reach to the frontal lobe. Their findings were recently replicated by other research groups [74], [75], hence the decreased dispersion in superior occipito-frontal fasciculus might not necessarily disagree with the previously reported hypothesis of the increased connectivity of psychosis in prefrontal regions. For the corpus callosum, considering the body of the region defined in JHU atlas, decreased dispersion might implicate decreased structural connectivity between the right and left hemispheres of the brain. Interestingly, in the genu of corpus callosum, which connects medial and lateral surfaces of the frontal lobes, none of the selected diffusion measures is found to be significant for the discrimination. We note that previous dMRI studies of the bipolar disease also reported abnormal change in corpus callosum [76], [77], where our data confirm this also with increased ADC, RD, and AD.

Considering brain WM labels defined in JHU atlas, our results are consistent with the results of Juelich atlas regions for the partially overlapping regions such as external capsule (partially overlaps with inferior occipito-frontal fascicle) and cingulum, where there is a significant increase in dispersion for the bipolar-healthy control groups comparison. However, as we observed decreased dispersion in the corticospinal tract of JHU atlas for the bipolar group, the change in dispersion is not significant for the region defined in the Juelich atlas, where the tract is defined as a bundle which connects brain stem and precentral gyrus in the frontal lobe. In other words, the regions are different from each other, such that in JHU atlas the label is located in the region of the brain stem, and the upper part of the tract is labeled as cerebral peduncle followed by internal capsule and corona radiata. Therefore, we considered all the subdivisions of

the corticospinal tract defined in JHU atlas together, such that significantly decreased dispersion is observed in corticospinal tract and superior corona radiata, except from that, the change in dispersion is not significant in the cerebral peduncles and internal capsule. This implies that decreased structural connectivity exists only for the lower and the upper part of the bundle. Our findings on the corticospinal tract is consistent with a recent study which reports reduced motor activity in a bipolar group [78].

Noting that the superior longitudinal fasciculus defined in Juelich atlas is smaller and located in the central part of the hemisphere compared to the region defined in JHU atlas, there was no significant difference between the groups considering the region in Juelich atlas. On the other hand, in the superior longitudinal fasciculus (defined in JHU atlas), which connects frontal, occipital, parietal, and temporal lobes, a decreased dispersion observed for the bipolar group suggests that there might be a decreased structural connectivity between the aforementioned lobes, which is also previously reported to be significant for the deficits in bipolar groups [77], [76], [79].

5. SEGMENTATION OF THE CINGULUM STRUCTURE USING DISPERSION MAP

To admit the technical motivation of the thesis, macroscopic dispersion map shows distinct contrast between certain white matter structures such as cingulum which is a partially coherent pathway interconnecting many cortex regions from posterior to anterior parts of the hemisphere. It runs superior to corpus callosum both at the right and left hemispheres. A part of the bundle is coherent to some extent from which few short association fibers run towards the cortex at certain regions. Recent studies subdivide the cingulum bundle into different parts considering multiple information resources including region of interest based tractography [80], [81]. Therefore tractogram is an important data to define cortical and subcortical regions that the cingulum bundle interconnects. Since macroscopic dispersion is a tractogram based measure, there is a bundle specific contrast in the dispersion map (Figure 5.1). In this chapter we proposed a framework for active contour based segmentation of the coherent region in the cingulum. The aimed region corresponds to the mid-anterior, mid-posterior, and post-dorsal neighbours of cingulate gyrus [82]. Therefore, quantitative performance of the segmentation results are compared to labels of cingulum at JHU atlas which covers the aimed region. Results are demonstrated also qualitatively supporting that the segmentation result could be used as a seed for tractography of the cingulum bundle.

5.1 Dataset

Experiments were performed using Human Connectome Project (HCP) dataset. 10 subjects were chosen among HCP 900 Subject Release with the following subject ids: [100610, 102311, 102816, 104416, 105923, 108323, 109123, 111312, 111514, 114823]. Siemens 3T Connectom scanner was used for imaging of diffusion and T1 weighted images having isotropic spacing (1.25 mm) and the image size of $145 \times 174 \times 145$. Diffusion weighted images have 18 $b \approx 0$ images and three different b-value shells ($b \approx 1000$, $b \approx 2000$, $b \approx 3000$) that each shell sphere was sampled in 90 different

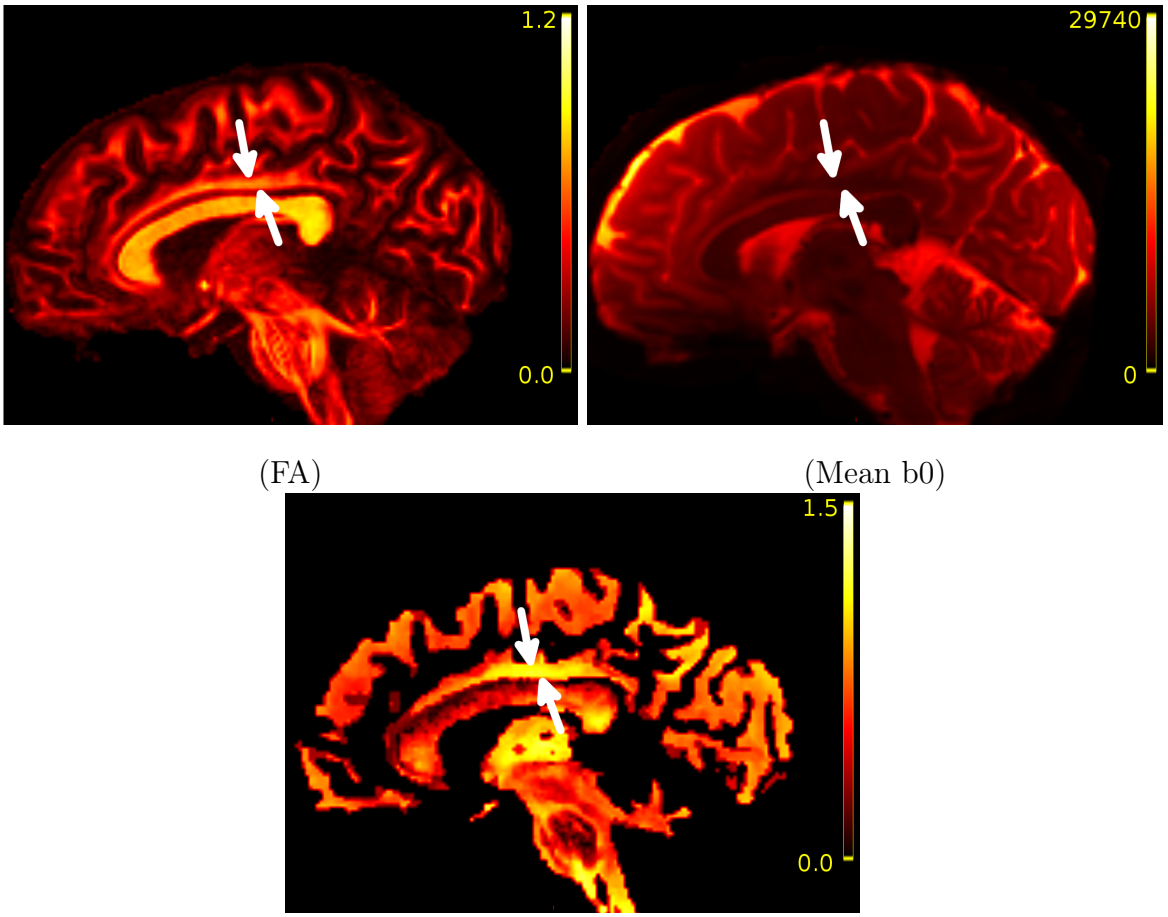

Figure 5.1 A comparison of the coherence (inverse dispersion) map in contrast to mean b0 and FA map.

directions. We used preprocessed images that are corrected for bias field, eddy current, and motion.

5.2 Segmentation framework

For segmentation of cingulum we used ITKSnap tool in which there is an implementation of active contour segmentation method [83]. The left and right cingulum were segmented separately. First, a box ROI covering all parts of the cingulum was located. Then, inside and outside cingulum regions were marked with two different label colors manually for a set of classification. As a result, a speed map was computed

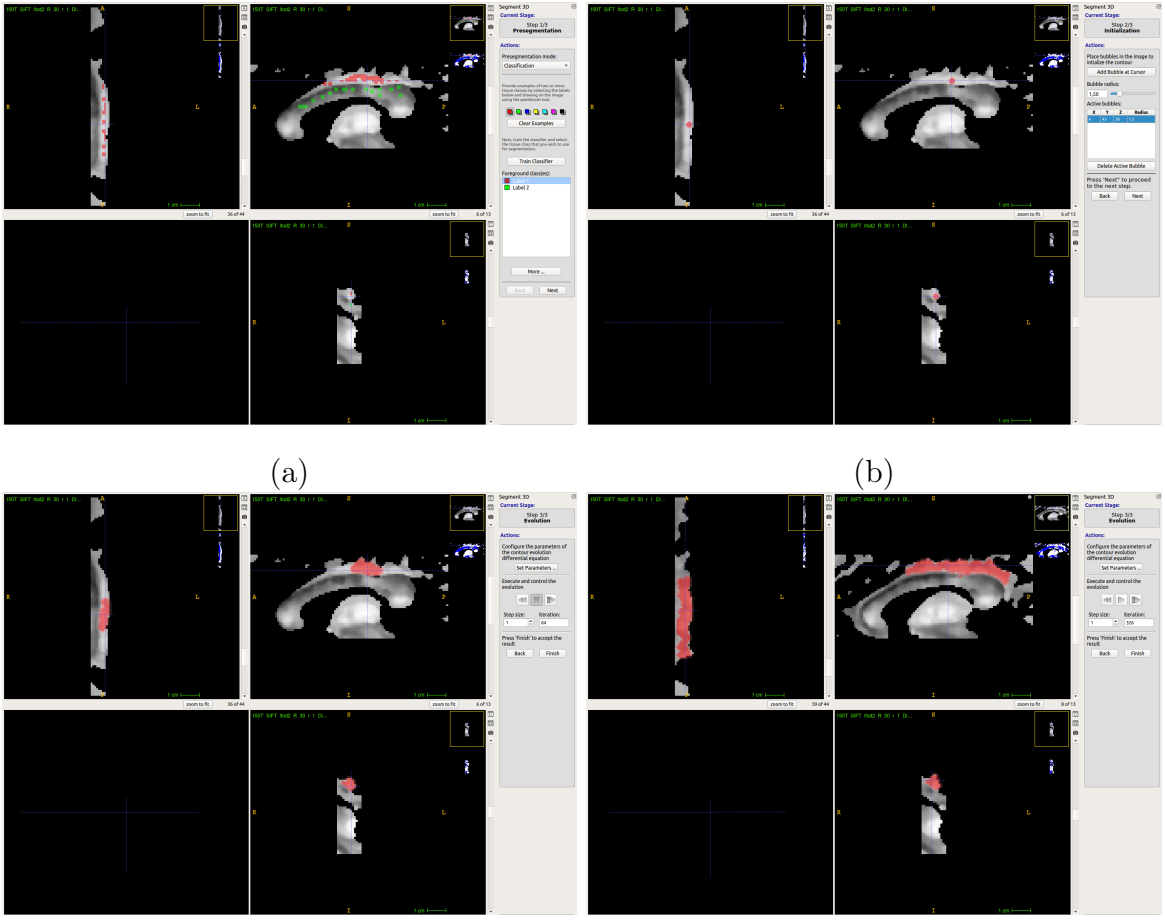

Figure 5.2 Active contour segmentation framework: (a) Pre-segmentation, (b) Spherical seed initialization, (c) Contour evolution step 64, (d) Contour evolution step 326.

and displayed to be used for contour evolution. Then a small seed contour is initialized on the cingulum. The next step is to start the evolution steps following the contour evolution using the Eq. 5.1, where C_t defines a contour at time step t, $g(\mathrm{I})$ is the speed image obtained from the gradient of the dispersion map (I), κ is the mean curvature of the contour, and $\overrightarrow{\eta}$ is the normal vector of the contour. We used default values for α and β as $\alpha = 1.0$ and $\beta = 0.2$

$$C_t = (\alpha g(\mathrm{I}) - \beta\kappa)\overrightarrow{\eta} \tag{5.1}$$

After certain evolution steps, where the step size is 1.0 mm, contour speed was slowed, and at about 300^{th} step the contour had its almost final shape which was saved as a segmentation result.

5.3 Results and Discussions

For the qualitative performance of the segmentation framework, all the segmentation maps were transformed to the MNI atlas space and a mean image of the maps were shown in Figure 5.3. Besides, overlap statistics were given in Table 5.1 which includes dice overlap $((2 * vol(A \cap B))/(vol(A) + vol(B)))$ metric comparing each segmentation with the cingulum region defined in JHU atlas [65]. These results show that the inverse dispersion (coherence) map could easily be used to segment mid-anterior, mid-posterior and post-dorsal parts of the cingulum bundle. Mean segmentation maps qualitatively similar to the JHU cingulum maps for both sides, however there is a left greater than right asymmetry in HCP dataset. Therefore, overlap ratio is greater in the right cingulum.

Aim of this segmentation framework is to demonstrate that there is a high dispersion contrast between the cingulum and its neighbouring structures such as corpus callosum. In addition, the anterior part of cingulum runs more dispersively that the dispersion is more higher in the mid part than the anterior or dorsal part of cingulum. It could be shown with the tractography of the cingulum that our segmentation framework could be used as a seed ROI to delineate the cingulum bundle from the whole brain tractogram. The proposed segmentation framework could also be followed on other coherent bundles such as the genu and the splenium of corpus callosum.

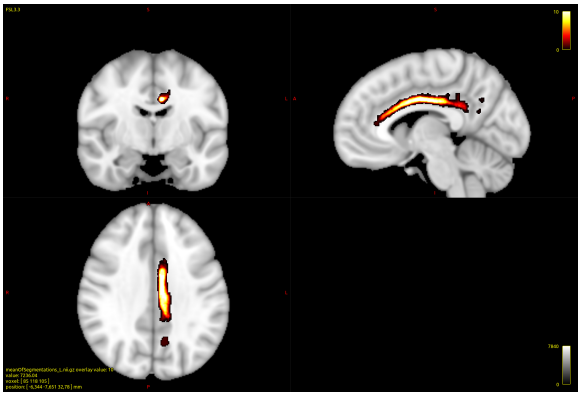

(a) Mean segmentation map (left)

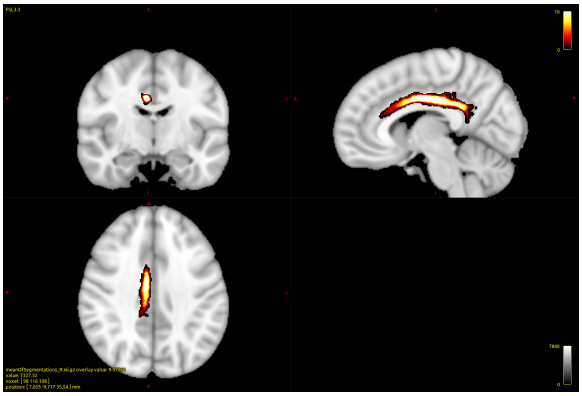

(b) Mean segmentation map (right)

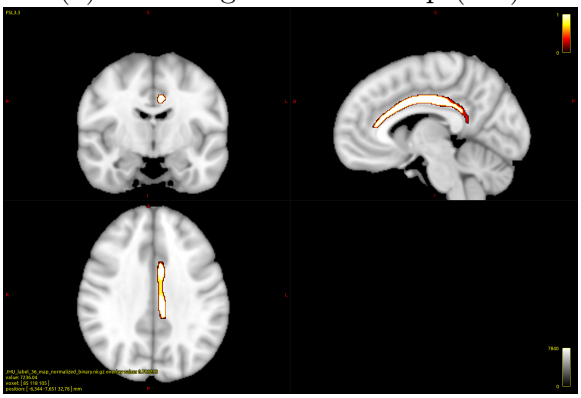

(c) Left cingulum

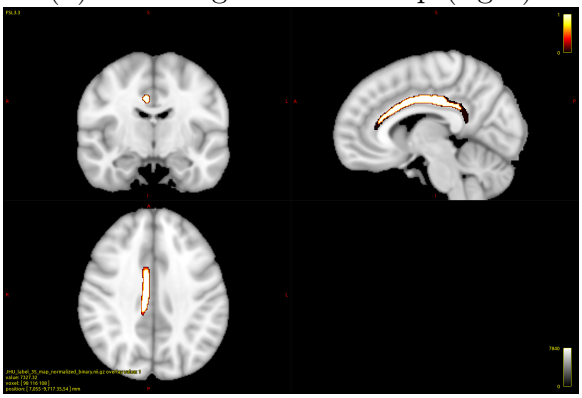

(d) Right cingulum

Figure 5.3 Mean segmentation image of 10 HCP Data.

Table 5.1
Overlap statistics of cingulum segmentation using inverse dispersion map.

Left Cingulum						
ID	Overlap	Seg. Vol.	JHU Vol.	Dice Coeff.	Overlap/(Seg.)	Overlap/JHU
100610	1044	2144	2751	0.4265	0.4869	0.3794
102311	984	2317	2751	0.3883	0.4246	0.3576
102816	993	1996	2751	0.4183	0.4974	0.3609
104416	1272	2942	2751	0.4468	0.4323	0.4623
105923	1180	2555	2751	0.4447	0.4618	0.4289
108323	846	1821	2751	0.37	0.4645	0.3075
109123	823	1535	2751	0.384	0.5361	0.2991
111312	1140	2252	2751	0.4557	0.5062	0.4143
111514	1180	2297	2751	0.4675	0.5137	0.4289
114823	746	1450	2751	0.3551	0.5144	0.2711
Mean Seg.	1629	3539	2751	0.5179	0.4602	0.5921
Right Cingulum						
ID	Overlap	Seg. Vol.	JHU Vol.	Dice Coeff.	Overlap/(Seg.)	Overlap/JHU
100610	1261	1906	2342	0.5936	0.6615	0.5384
102311	843	1465	2342	0.4428	0.5754	0.3599
102816	956	1886	2342	0.4522	0.5068	0.4081
104416	741	1373	2342	0.3989	0.5396	0.3163
105923	882	1515	2342	0.4573	0.5821	0.3766
108323	1034	1511	2342	0.5367	0.6843	0.4415
109123	1063	1706	2342	0.5251	0.623	0.4538
111312	1267	2283	2342	0.5478	0.5549	0.5409
111514	1085	1771	2342	0.5275	0.6126	0.4632
114823	851	1458	2342	0.4478	0.5836	0.3633
Mean Seg.	1655	3227	2342	0.5943	0.5128	0.7066

6. CONCLUSION AND FUTURE PERSPECTIVES

In this thesis we first addressed quantification issues of the brain wiring diagram and we proposed that macroscopic characteristics of the brain tractogram would provide information about abnormal clinical cases which are difficult to diagnose using imaging modalities. Characteristics of the brain white matter fibers were mostly inferred using the statistics of the microscopic diffusion measures obtained from the delineated bundle of interest discarding the complex and sometimes distinctively inseparable shape characteristics. Besides it is sometimes impossible to label a voxel where there are crossing regions. Therefore we have demonstrated a method to quantify macro-structural interconnectivity for a given voxel using its macroscopic dispersion profile without considering its anatomical label. Hence, the proposed method for the macroscopic dispersion statistics employed for the whole WM voxels to compute a novel structural map that is named as the macroscopic dispersion map of the brain. Our contributions have both clinical and technical outcomes.

As a clinical application, macroscopic dispersion reveals that the macroscopic interconnectivity, which could not directly be inferred in local diffusion measurements, might be different in the case of psychosis. In Chapter 4, it is shown that the macroscopic dispersion changes might be a certain characteristic of bipolar disorder. Increased or decreased macroscopic dispersion might be related to the functioning mechanisms of the abnormalities in such cases. In addition, similar changes were also observed in schizophrenia as we have observed slightly increased macroscopic dispersion in the right cingulum.

The macroscopic observations reported in this thesis motivate us to have further investigations in a large dataset, such as HCP dataset, so that we could observe more reliable macroscopic dispersion statistics of a normal cohort for each bundle. This study would be a reference for normal values of macroscopic dispersion to compare with abnormal cases.

Another further contribution of the proposed method would be observed if it is used in a disease classification problem as an input together with other neuroimaging markers. The results of such an experiment would demonstrate the performance of the proposed measure when it is combined with the microscopic measures.

There are many clinical parameters, such as severity of the disease, duration from the onset of the disease, and medication usage, which should be considered together with the macroscopic dispersion changes to investigate further details of the macroscopic progression of the diseases with the clinical observations.

Distinctive geodesic shape of the brain white matter fibers is also a unique source for the technical applications. Our findings suggest that the proposed macroscopic dispersion measure is an informative map for technical challenges. We emphasized its contrast characteristics compared to local measures in Chapter 5 for the cingulum by proposing an active contour based segmentation framework which uses solely the macroscopic dispersion map. Since the parcellation of the brain in an atlas is an average result from many subjects, it could not be considered as ground truth but one further investigation would be to compare the segmentation results with the expert guided segmentation of the cingulum. Another qualitative validation study could be performed considering the segmentation results for seeding the tractography of the cingulum bundle.

The macroscopic dispersion becomes more than 1.0 at points having a complex fiber profile. For these cases the proposed iterative end point clustering approach might produce uncertain results and it would require an optimization scheme to perform several initialization steps to optimize the clustering using the minimized macroscopic dispersion. This investigation might be necessary if a filtering is required for the produced dispersion map.

Overall, we have demonstrated a macroscopic biomarker which should also be informative for other clinical applications where there might be white matter abnormalities such as Parkinson's disease. We also emphasize that there might be future

advances in macroscopic measures of tractogram. These measures should improve the understanding of the characteristics with the neurological meaning and its sensitivity to the changes in white matter. The tractogram is mostly sampled as fibers defined with a set of consecutive points. There might be new sampling and transform models that produce high dimensional macroscopic characteristics of the fibers. Definition of smart convolution kernels for the tractogram might also contribute to the technical advances as needed in the deep learning methods.

APPENDIX A. GAUSSIAN PROCESS BASED MACROSCOPIC DISPERSION

Gaussian process based representation of the fiber leads to a different kind of dispersion computation [84], such that the normalized inner product of two Gaussian processes ($< G_i, G_j >$) gives, oppositely, a coherence measure that ranges from 0.0 to 1.0. G_i is the Gaussian process representation of the truncated fiber i which is in the set of fibers passing through a voxel. For the Gaussian process based approach, we defined dispersion in Eq. A.1 as the average value of all pairwise coherence values subtracted from 1.0.

$$\delta_g = 1.0 - \frac{1}{N(N-1)/2} \sum_{i=0}^{N-1} \sum_{j=i+1}^{N-1} \frac{< G_i, G_j >}{\|G_i\| \|G_j\|} \tag{A.1}$$

We note that, for the experiments depicted in this chapter, end points based dispersion was defined without considering a normalization factor of R as we used in Section 3.1. Here, the end points based dispersion was defined as in Eq. A.2.

$$\delta_p = \frac{1}{N} \sum_{i=0}^{N-1} \frac{1}{2} (\|(X_i^{(s)} - X_c^{(s)}\|_2 + \|(X_i^{(e)} - X_c^{(e)}\|_2) \tag{A.2}$$

Figures [A.2,A.3,A.4,A.5] shows the dispersion maps of the datasets depicted in Figure A.1 for different values of the tuning parameters: radius of truncation sphere, R, and the radius of sphere ROI, r. The increasing value of r blured the dispersion map by including more number of fibers passing through the neighbouring voxels. Whereas the increasing value of R increased the contrast of the dispersion map. Therefore, we need to truncate fibers to discard the effect of fiber length in dispersion measure. Note

that, both of the proposed approaches for the dispersion measure were independent of the fiber length, however the fiber length indirectly increases the dispersion contrast. Synthetic datasets were tested for both end points based and GP based approaches and the results were similar but there was a limiting issue with the computation times, such that GP based approach requires more computation time. For example, the computation of a dispersion map on a crossing dataset was completed in ≈ 10 seconds and ≈ 14 minutes respectively for end points based and GP based approaches.

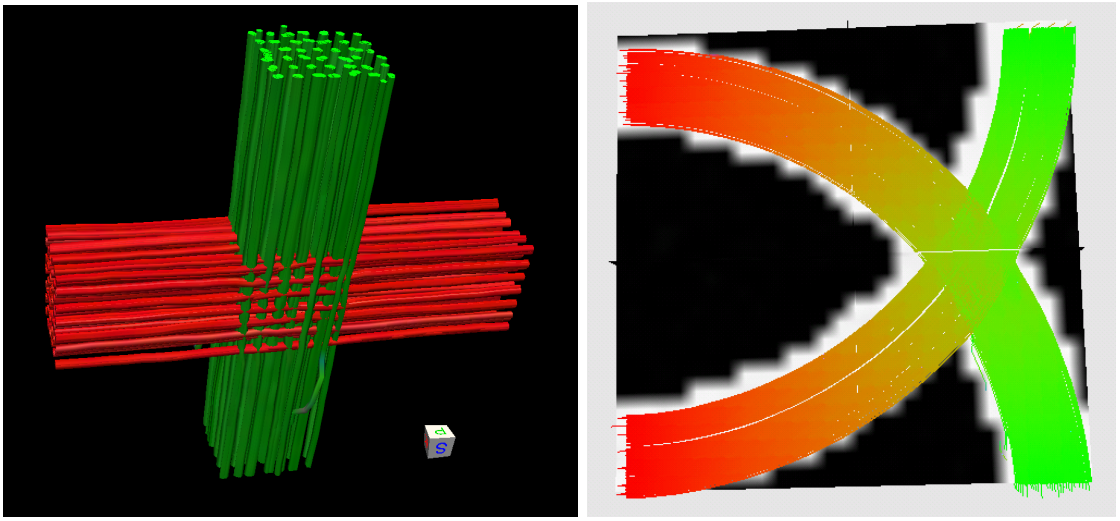

(90-degree crossing fibers) (Crossing fibers)

Figure A.1 Two different crossing fibers datasets.

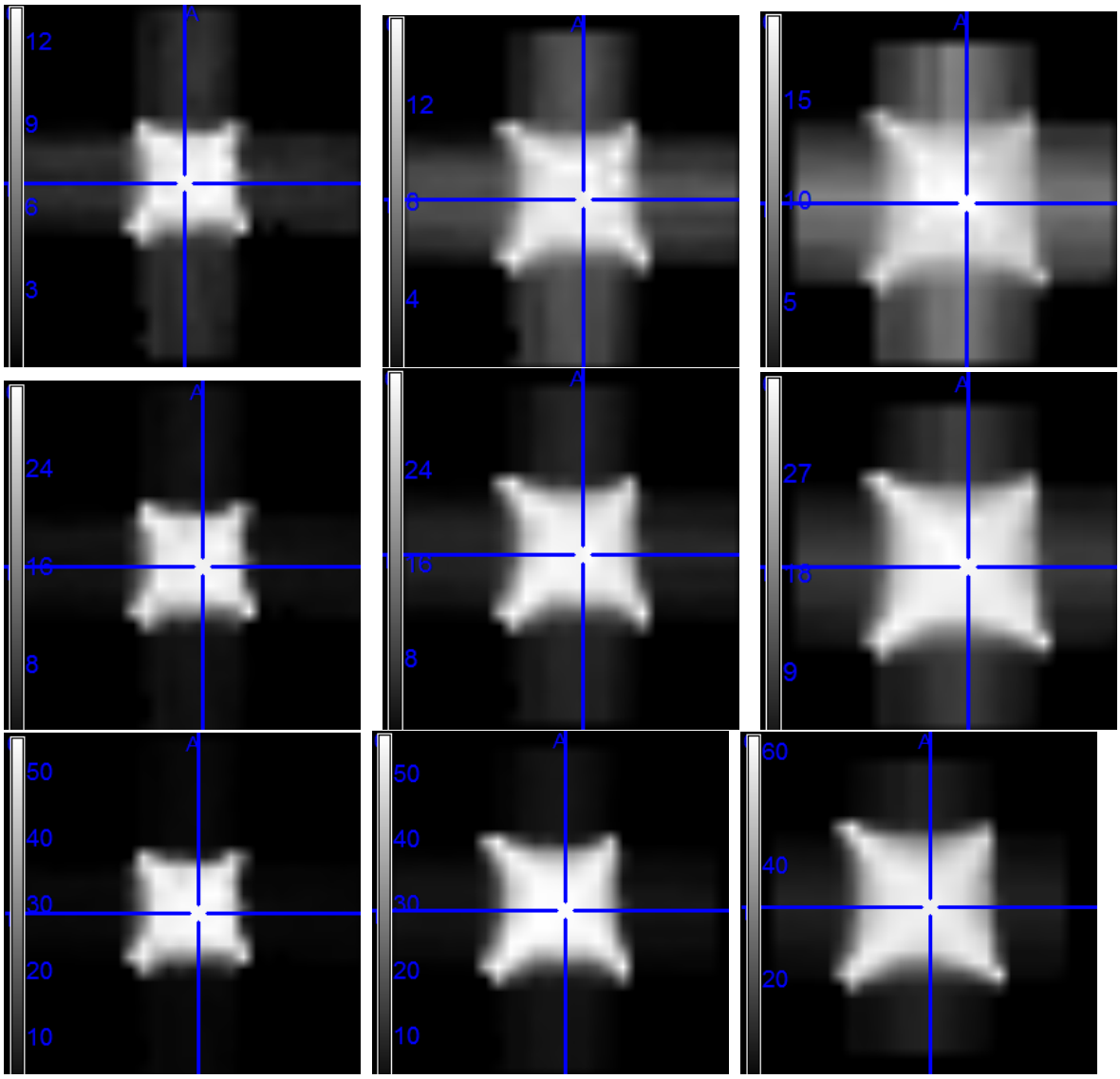

Figure A.2 90 degree crossing fibers. Dispersion maps are obtained by the end points based approach. Each row image is obtained by setting the radius of truncation sphere, $R \in \{4, 6, 8\}$ (top to bottom), and each column image is obtained by setting the radius of sphere ROI $r \in \{1, 2, 3\}$ (left to right).

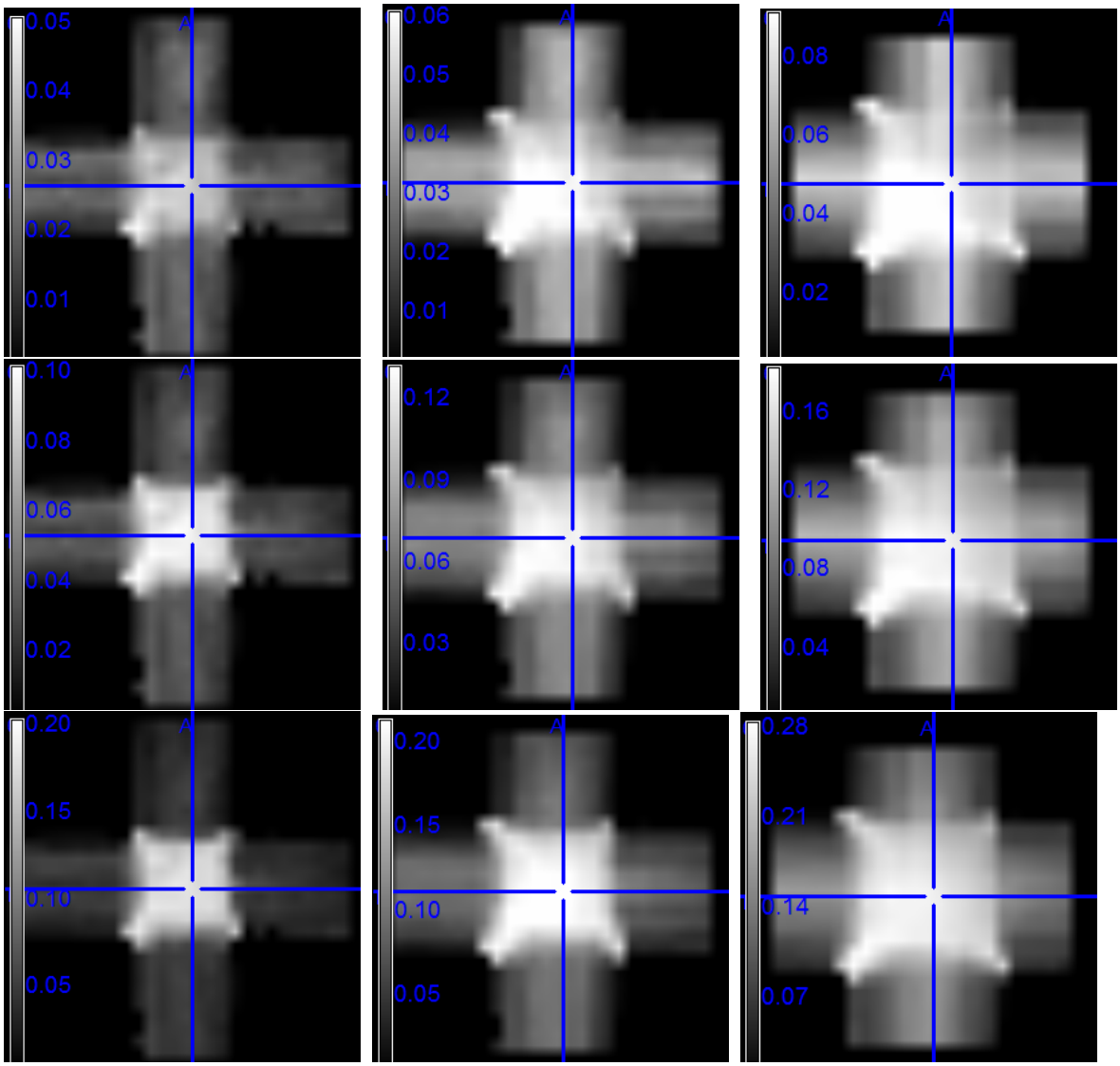

Figure A.3 90 degree crossing fibers. Dispersion maps are obtained by the GP based approach. Each row image is obtained by setting the radius of truncation sphere, $R \in \{4, 6, 8\}$ (top to bottom), and each column image is obtained by setting the radius of sphere ROI $r \in \{1, 2, 3\}$ (left to right).

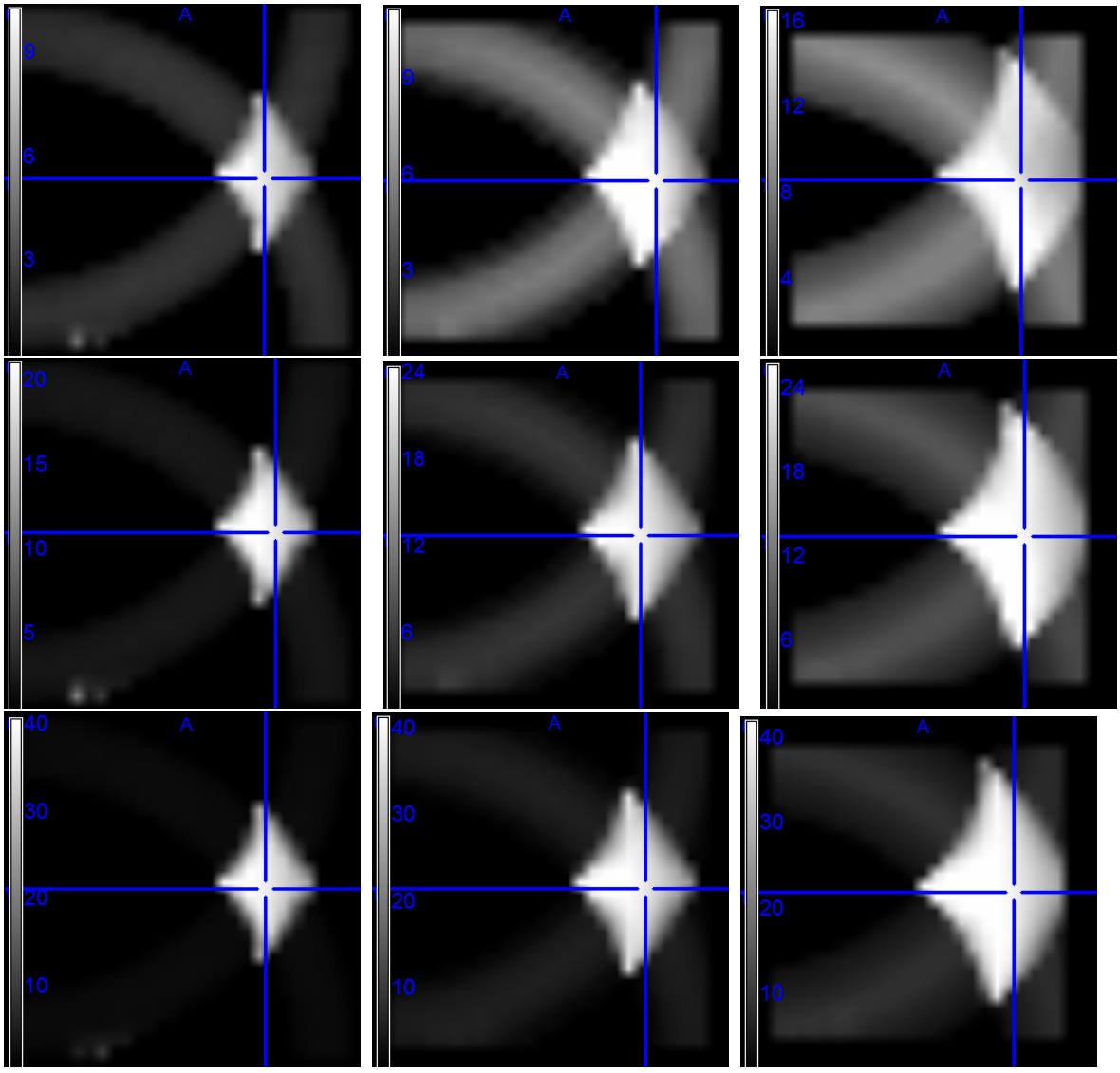

Figure A.4 Crossing fibers. Dispersion maps are obtained by the end points based approach. Each row image is obtained by setting the radius of truncation sphere, $R \in \{4, 6, 8\}$ (top to bottom), and each column image is obtained by setting the radius of sphere ROI $r \in \{1, 2, 3\}$ (left to right).

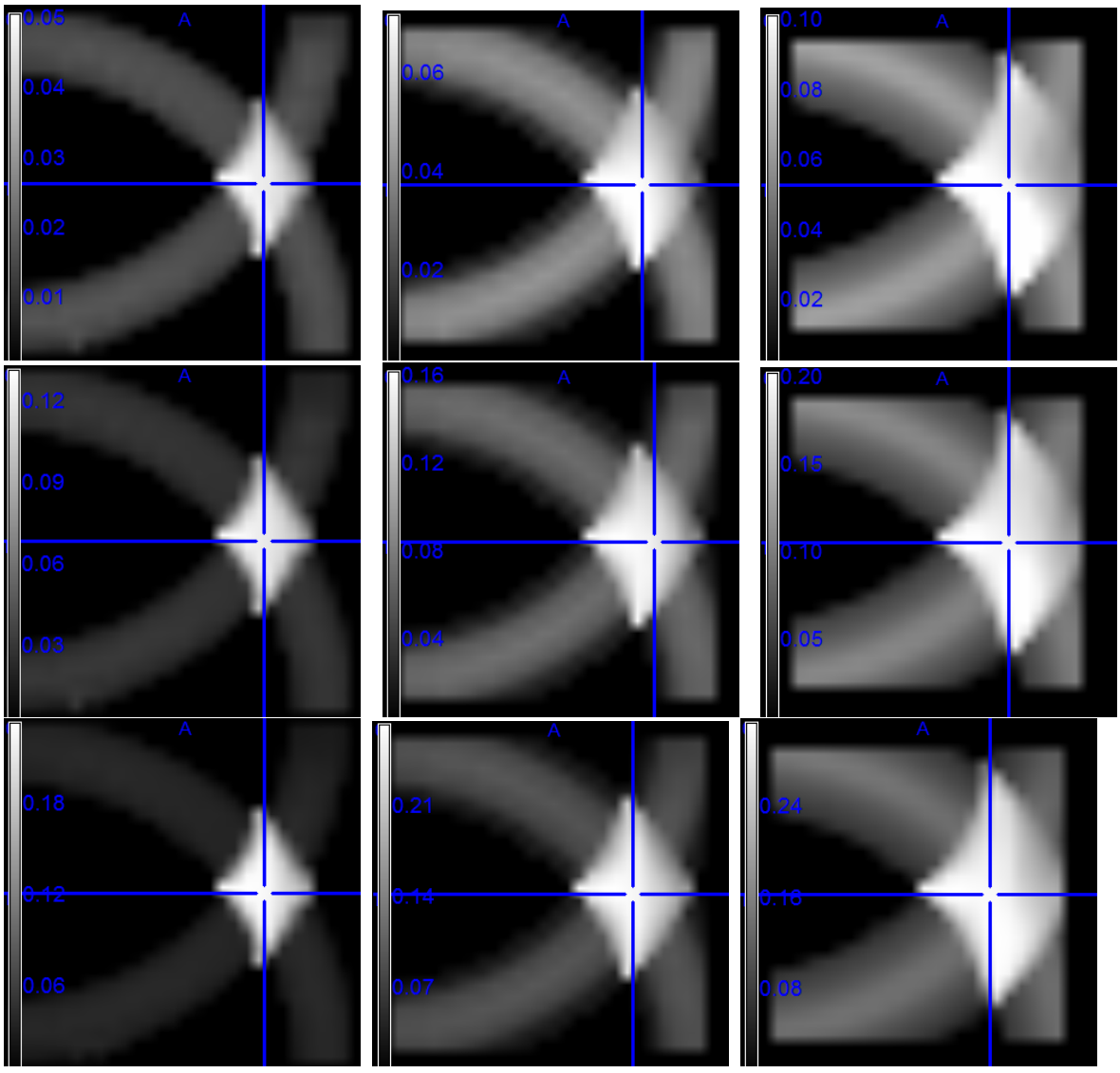

Figure A.5 Crossing fibers. Dispersion maps are obtained by the GP based approach. Each row image is obtained by setting the radius of truncation sphere, $R \in \{4, 6, 8\}$ (top to bottom), and each column image is obtained by setting the radius of sphere ROI $r \in \{1, 2, 3\}$ (left to right).

APPENDIX B. A TOOL FOR THE MACROSCOPIC DISPERSION

Recently we released a publicly available graphical user interface tool with the name of "BWMExplorer" for the proposed macroscopic dispersion. It can be downloaded from https://bitbucket.org/_ali_demir/. It requires a reference nifti image at diffusion space and a tractogram file in TRK format. Then, the program computes the macroscopic dispersion map and displays 3D fibers of pointed voxel together with the computed macroscopic dispersion value printed on a text box. Right click on the axial, sagittal or coronal MR images update the 3D view and compute and display dispersion statistics for the on clicked voxel. "Ctrl+S" key press opens a dialog to save dispersion map in nifti format.

There are different view options for the fibers of a voxel to view on or off the truncation sphere, end point spheres, and trimmed or untrimmed fibers (Figure B.3)

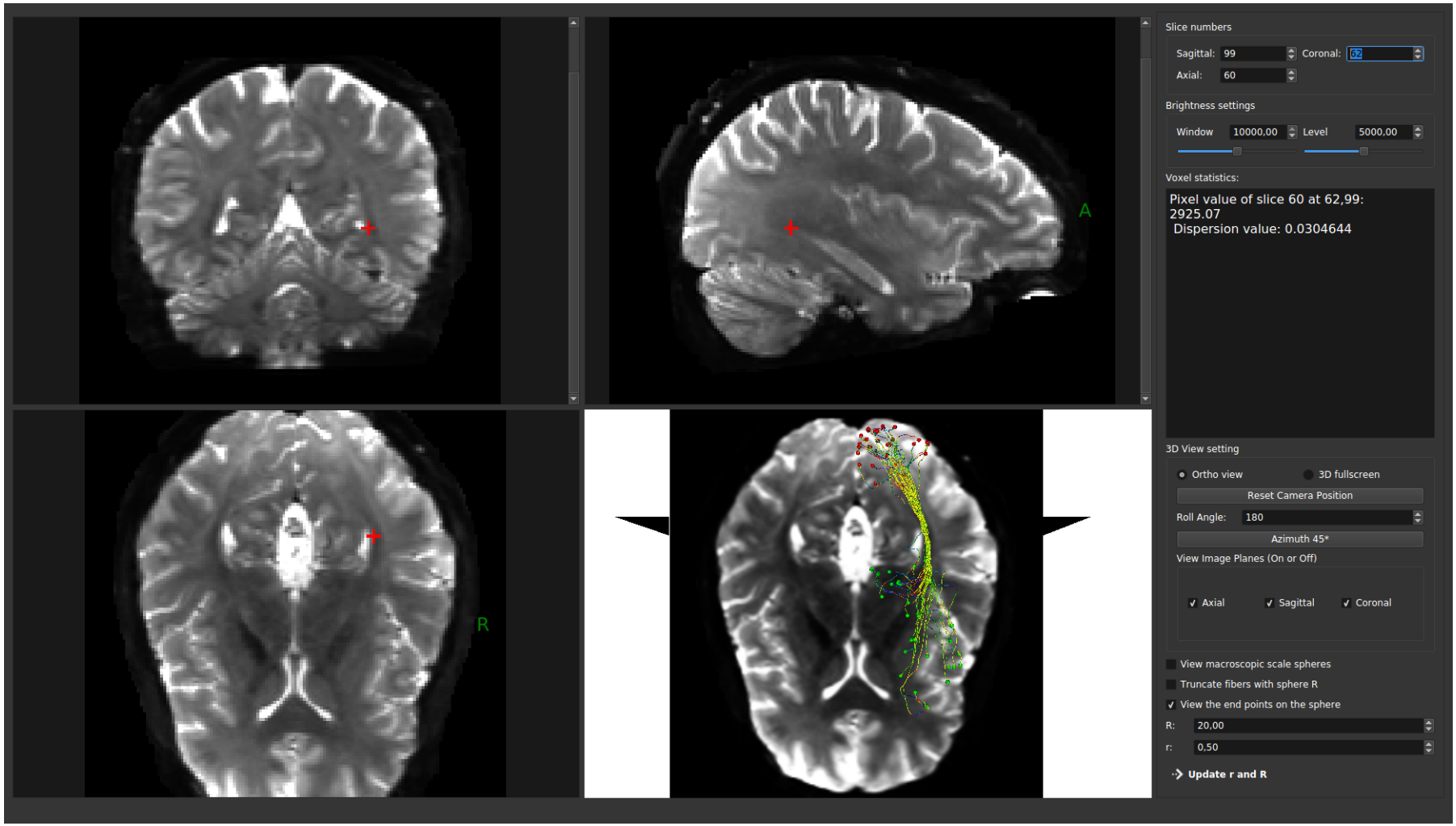

Figure B.1 Untruncated fibers.

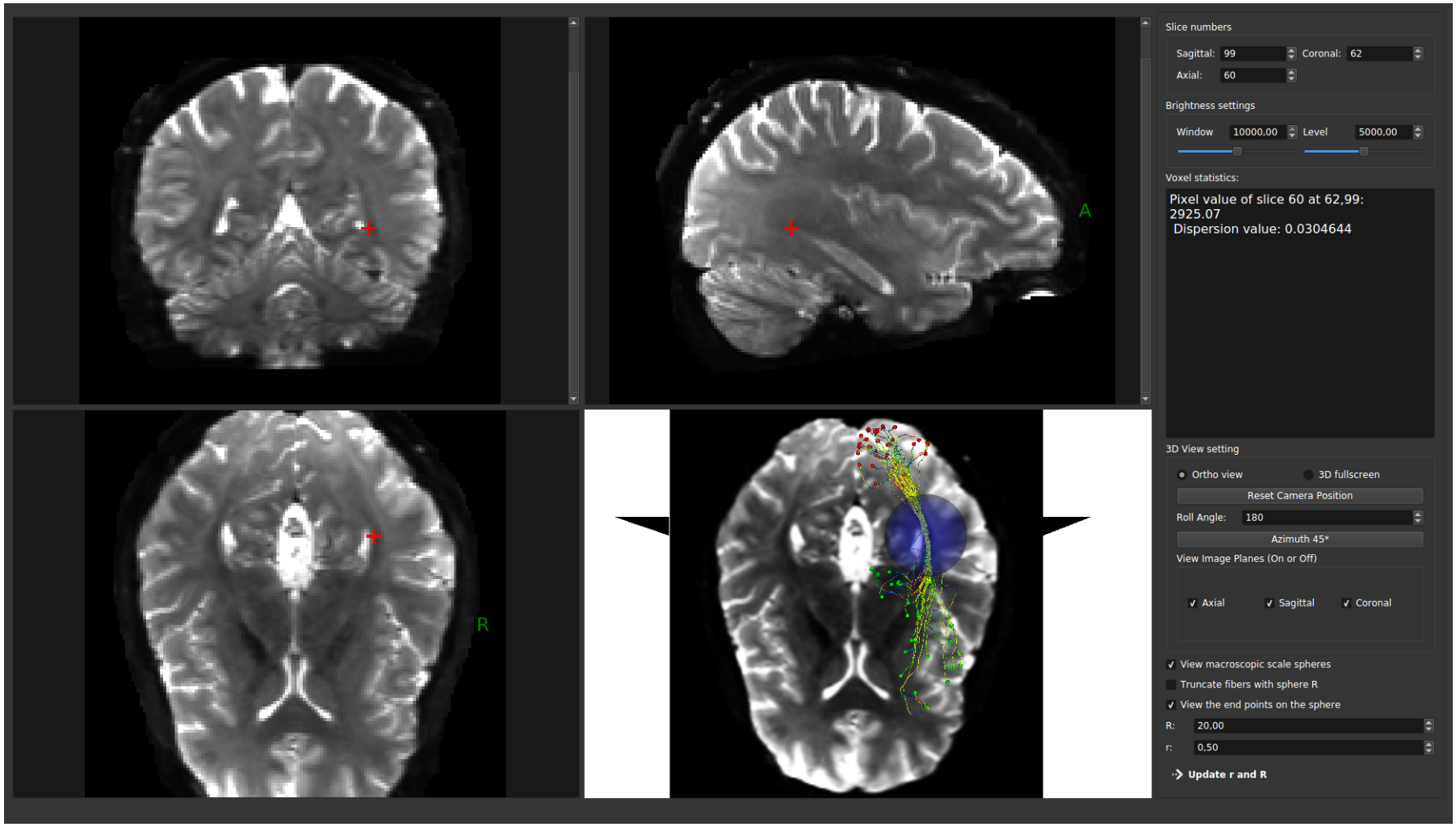

Figure B.2 Untruncated fibers with truncation sphere.

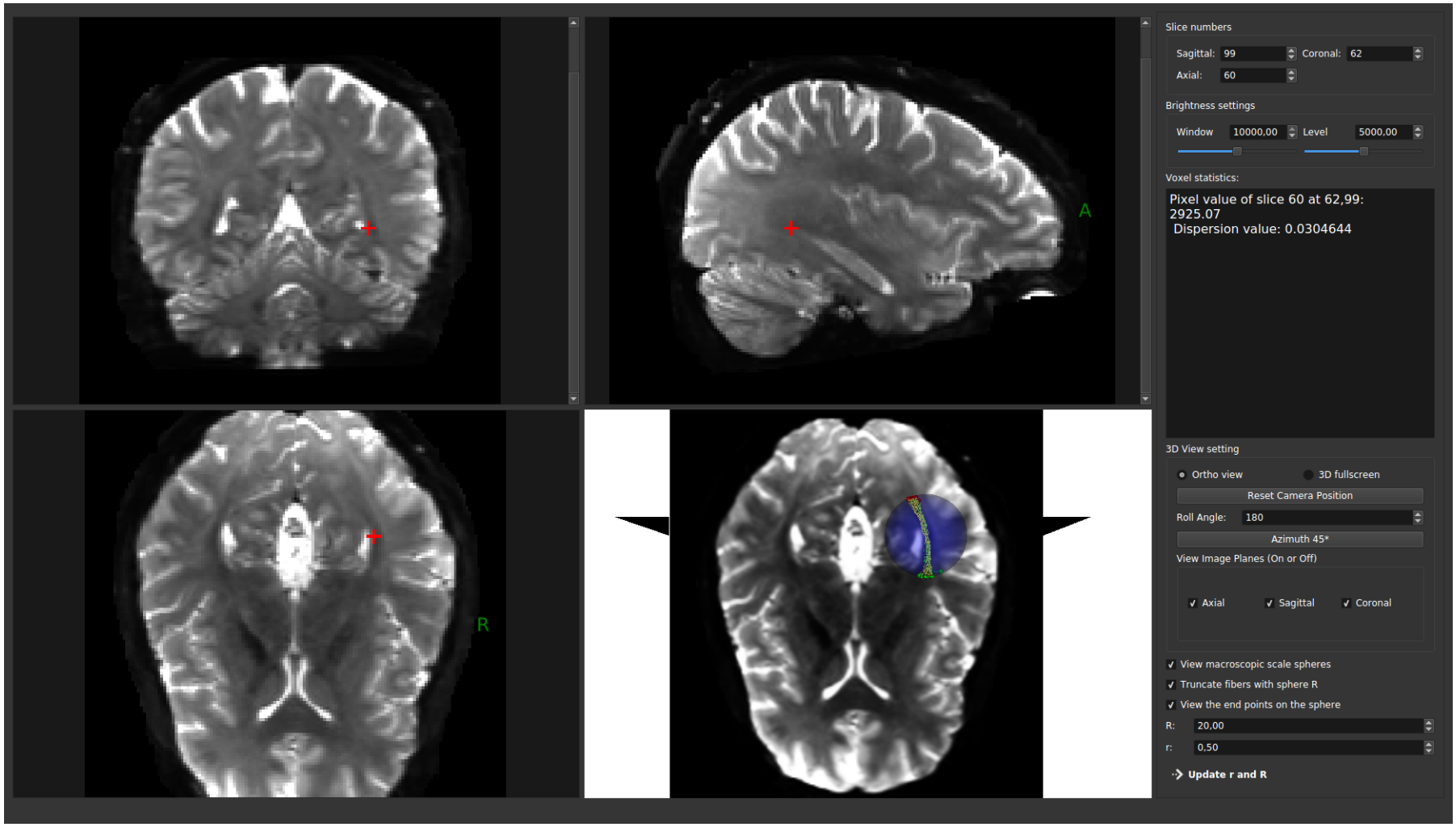

Figure B.3 Truncated fibers with truncation sphere.

APPENDIX C. LIST OF PUBLICATIONS PRODUCED FROM THE THESIS

1. A macro-structural dispersion characteristic of brain white matter and its application to bipolar disorder, A. Demir, M. Özkan, A. M. Uluğ, " *IEEE Transactions on Biomedical Engineering*, Vol. 00, pp. 1-8, June, 2020.

REFERENCES

1. Johansen-Berg, H., "Human connectomics - what will the future demand?," *NeuroImage*, Vol. 80, no. 0, pp. 541 – 544, 2013.

2. de Reus, M. A., and M. P. van den Heuvel, "The parcellation-based connectome: Limitations and extensions," *NeuroImage*, Vol. 80, no. 0, pp. 397 – 404, 2013.

3. Lichtman, J. W., and J. R. Sanes, "Ome sweet ome: what can the genome tell us about the connectome?," *Current Opinion in Neurobiology*, Vol. 18, no. 3, pp. 346 – 353, 2008.

4. Catani, M., M. T. de Schotten, D. Slater, and F. Dell'Acqua, "Connectomic approaches before the connectome," *NeuroImage*, Vol. 80, no. 0, pp. 2 – 13, 2013.

5. Maddah, M., A. U. J. Mewes, S. Haker, W. E. L. Grimson, and S. K. Warfield, "Automated atlas-based clustering of white matter fiber tracts from dtmri," in *Proceedings of the 8th international conference on Medical Image Computing and Computer-Assisted Intervention - Volume Part I*, MICCAI'05, pp. 188–195, Berlin, Heidelberg: Springer-Verlag, 2005.

6. Margulies, D. S., J. Böttger, A. Watanabe, and K. J. Gorgolewski, "Visualizing the human connectome," *NeuroImage*, Vol. 80, no. 0, pp. 445 – 461, 2013.

7. Passingham, R. E., "What we can and cannot tell about the wiring of the human brain," *NeuroImage*, Vol. 80, no. 0, pp. 14 – 17, 2013.

8. O'Donnell, L. J., A. J. Golby, and C.-F. Westin, "Fiber clustering versus the parcellation-based connectome," *NeuroImage*, Vol. 80, no. 0, pp. 283 – 289, 2013.

9. Sporns, O., "The human connectome: Origins and challenges," *NeuroImage*, Vol. 80, no. 0, pp. 53 – 61, 2013.

10. Axer, M., K. Amunts, D. Grässel, C. Palm, J. Dammers, H. Axer, U. Pietrzyk, and K. Zilles, "A novel approach to the human connectome: Ultra-high resolution mapping of fiber tracts in the brain," *NeuroImage*, Vol. 54, no. 2, pp. 1091 – 1101, 2011.

11. Basser, P., J. Mattiello, and D. Lebihan, "Estimation of the effective self-diffusion tensor from the nmr spin echo," *Journal of Magnetic Resonance, Series B*, Vol. 103, no. 3, pp. 247 – 254, 1994.

12. Barmpoutis, A., M. S. Hwang, D. Howland, J. R. Forder, and B. C. Vemuri, "Regularized positive-definite fourth order tensor field estimation from DW-MRI," *NeuroImage*, Vol. 45, no. 1 Suppl., pp. S153 – S162, 2009.

13. Tuch, D., "Q-ball imaging," *Magnetic Resonance in Medicine*, Vol. 52, no. 6, pp. 1358–1372, 2004.

14. Fillard, P., M. Descoteaux, A. Goh, S. Gouttard, B. Jeurissen, J. Malcolm, A. Ramirez-Manzanares, M. Reisert, K. Sakaie, F. Tensaouti, T. Yo, J.-F. Mangin, and C. Poupon, "Quantitative evaluation of 10 tractography algorithms on a realistic diffusion MR phantom," *Neuroimage*, Vol. 56, no. 1, pp. 220–234, 2011.

15. Smith, R. E., J.-D. Tournier, F. Calamante, and A. Connelly, "Anatomically-constrained tractography: Improved diffusion {MRI} streamlines tractography through effective use of anatomical information," *NeuroImage*, Vol. 62, no. 3, pp. 1924 – 1938, 2012.

16. Smith, S., M. Jenkinson, H. Johansen-Berg, D. Rueckert, T. Nichols, C. Mackay, K. Watkins, O. Ciccarelli, M. Cader, P. Matthews, and T. Behrens, "Tract-based spatial statistics: voxelwise analysis of multi-subject diffusion data," *NeuroImage*, Vol. 31, no. 4, pp. 1487–1505, 2006.

17. Teipel, S. J., W. Bayer, G. E. Alexander, Y. Zebuhr, D. Teichberg, L. Kulic, M. B. Schapiro, H. J. Möller, S. I. Rapoport, and H. Hampel, "Progression of corpus callosum atrophy in alzheimer disease," *Archives of Neurology*, Vol. 59, no. 2, pp. 243–248, 2002.

18. Laule, C., V. Pavlova, E. Leung, G. Zhao, A. L. MacKay, P. Kozlowski, A. L. Traboulsee, D. K. Li, and G. R. Moore, "Diffusely abnormal white matter in multiple sclerosis: Further histologic studies provide evidence for a primary lipid abnormality with neurodegeneration," *Journal of Neuropathology and Experimental Neurology*, Vol. 72, no. 1, pp. 42–52, 2013.

19. Batchelor, P., F. Calamante, J. Tournier, D. Atkinson, D. Hill, and A. Connelly, "Quantification of the shape of fiber tracts," *Magnetic Resonance in Medicine*, Vol. 55, no. 4, pp. 894–903, 2006.

20. Corouge, I., P. T. Fletcher, S. Joshi, S. Gouttard, and G. Gerig, "Fiber tract-oriented statistics for quantitative diffusion tensor mri analysis," *Medical Image Analysis*, Vol. 10, pp. 786–798, 2006.

21. Ding, Z., J. Gore, and A. Anderson, "Classification and quantification of neuronal fiber pathways using diffusion tensor MRI," *Magnetic Resonance in Medicine*, Vol. 49, no. 4, pp. 716–721, 2003.

22. O'Donnell, L., and C.-F. Westin, "Automatic tractography segmentation using a high-dimensional white matter atlas," *IEEE Trans. Med. Imaging*, Vol. 26, pp. 1562–1575, 2007.

23. Maddah, M., W. E. L. Grimson, S. K. Warfield, and W. M. Wells, "A unified framework for clustering and quantitative analysis of white matter fiber tracts," *Medical Image Analysis*, Vol. 12, no. 2, pp. 191 – 202, 2008.

24. Demir, A., and H. Cetingul, "Sequential hierarchical agglomerative clustering of white matter fiber pathways," *Biomedical Engineering, IEEE Transactions on*, Vol. PP, no. 99, pp. 1–1, 2015.

25. Mangin, J.-F., P. Fillard, Y. Cointepas, D. L. Bihan, V. Frouin, and C. Poupon, "Toward global tractography," *NeuroImage*, Vol. 80, no. 0, pp. 290 – 296, 2013.

26. Fillard, P., C. Poupon, and J.-F. Mangin, "A novel global tractography algorithm based on an adaptive spin glass model," in *Med Image Comput Comput Assist Interv.*, pp. 927–34, Dec 2009.

27. Kingsley, P. B., "Introduction to diffusion tensor imaging mathematics: Part ii. anisotropy, diffusion-weighting factors, and gradient encoding schemes," *Concepts in Magnetic Resonance Part A*, Vol. 28A, no. 2, pp. 123–154, 2006.

28. Uluğ, A. M., and P. C. van Zijl, "Orientation-independent diffusion imaging without tensor diagonalization: Anisotropy definitions based on physical attributes of the diffusion ellipsoid," *Journal of Magnetic Resonance Imaging*, Vol. 9, no. 6, pp. 804–813, 1999.

29. Gibbard, C. R., J. Ren, K. K. Seunarine, J. D. Clayden, D. H. Skuse, and C. A. Clark, "White matter microstructure correlates with autism trait severity in a combined clinicalâcontrol sample of high-functioning adults," *NeuroImage: Clinical*, Vol. 3, no. 0, pp. 106 – 114, 2013.

30. Price, G., M. Cercignani, G. J. Parker, D. R. Altmann, T. R. Barnes, G. J. Barker, E. M. Joyce, and M. A. Ron, "Abnormal brain connectivity in first-episode psychosis: A diffusion mri tractography study of the corpus callosum," *NeuroImage*, Vol. 35, no. 2, pp. 458 – 466, 2007.

31. Ameis, S. H., and M. Catani, "Altered white matter connectivity as a neural substrate for social impairment in autism spectrum disorder," *Cortex*, Vol. 62, no. Supplement C, pp. 158 – 181, 2015. Special issue: The clinical anatomy of the limbic lobe and connected structures.

32. Rostowsky, K. A., A. S. Maher, and A. Irimia, "Macroscale white matter alterations due to traumatic cerebral microhemorrhages are revealed by diffusion tensor imaging," *Frontiers in Neurology*, Vol. 9, p. 948, 2018.

33. Rau, Y.-A., S.-M. Wang, J.-D. Tournier, S.-H. Lin, C.-S. Lu, Y.-H. Weng, Y.-L. Chen, S.-H. Ng, S.-W. Yu, Y.-M. Wu, C.-C. Tsai, and J.-J. Wang, "A longitudinal fixel-based analysis of white matter alterations in patients with parkinson's disease," *NeuroImage: Clinical*, Vol. 24, p. 102098, 2019.

34. Paolini, P., R. Sabbadini, K. Roos, and R. Baskin, "Sarcomere length dispersion in single skeletal muscle fibers and fiber bundles," *Biophysical Journal*, Vol. 16, no. 8, pp. 919–930, 1976.

35. Vandermosten, M., H. Poelmans, S. Sunaert, P. Ghesquière, and J. Wouters, "White matter lateralization and interhemispheric coherence to auditory modulations in normal reading and dyslexic adults," *Neuropsychologia*, Vol. 51, no. 11, pp. 2087 – 2099, 2013.

36. Sotiropoulos, S. N., T. E. Behrens, and S. Jbabdi, "Ball and rackets: Inferring fiber fanning from diffusion-weighted MRI," *NeuroImage*, Vol. 60, no. 2, pp. 1412 – 1425, 2012.

37. Sethi, A., S. Sarkar, F. DellÁcqua, E. Viding, M. Catani, D. G. Murphy, and M. C. Craig, "Anatomy of the dorsal default-mode network in conduct disorder: Association with callous-unemotional traits," *Developmental Cognitive Neuroscience*, Vol. 30, pp. 87 – 92, 2018.

38. Faria, A. V., J. Crawford, C. Ye, J. Hsu, A. Kenkare, D. Schretlen, and A. Sawa, "Relationship between neuropsychological behavior and brain white matter in first-episode psychosis," *Schizophrenia Research*, Vol. 208, pp. 49 – 54, 2019.

39. Puglisi, G., H. Howells, T. Sciortino, A. Leonetti, M. Rossi, M. Conti Nibali, L. Gabriel Gay, L. Fornia, A. Bellacicca, L. Viganó, L. Simone, M. Catani, G. Cerri, and L. Bello, "Frontal pathways in cognitive control: direct evidence from intraoperative stimulation and diffusion tractography," *Brain*, Vol. 142, pp. 2451–2465, 07 2019.

40. Splittgerber, R., *Snell's Clinical Neuroanatomy*, Wolters Kluwer Health, 2018.

41. van Middendorp, J. J., G. M. Sanchez, and A. L. Burridge, "The edwin smith papyrus: a clinical reappraisal of the oldest known document on spinal injuries," *European spine journal : official publication of the European Spine Society, the European Spinal Deformity Society, and the European Section of the Cervical Spine Research Society*, Vol. 19, pp. 1815–1823, November 2010.

42. Türe, U., M. G. Yaşargil, A. H. Friedman, and O. Al-Mefty, "Fiber Dissection Technique: Lateral Aspect of the Brain," *Neurosurgery*, Vol. 47, pp. 417–427, 08 2000.

43. Carr, H. Y., and E. M. Purcell, "Effects of diffusion on free precession in nuclear magnetic resonance experiments," *Phys. Rev.*, Vol. 94, pp. 630–638, May 1954.

44. Hahn, E. L., "Spin echoes," *Phys. Rev.*, Vol. 80, pp. 580–594, Nov 1950.

45. Lauterbur, P., "Image formation by induced local interactions: Examples employing nuclear magnetic resonance," *Nature*, Vol. 242, pp. 190–191, 1973.

46. Mansfield, P., and A. A. Maudsley, "Medical imaging by nmr," *The British Journal of Radiology*, Vol. 50, no. 591, pp. 188–194, 1977.

47. Brewer, R. G., and E. L. Hahn, "Atomic memory," *Scientific American*, Vol. 251, no. 6, pp. 50–57, 1984.

48. Stejskal, E. O., and J. E. Tanner, "Spin diffusion measurements: Spin echoes in the presence of a timeâdependent field gradient," *The Journal of Chemical Physics*, Vol. 42, no. 1, pp. 288–292, 1965.

49. King, M. D., J. Houseman, S. A. Roussel, N. Van Bruggen, S. R. Williams, and D. G. Gadian, "q-space imaging of the brain," *Magnetic Resonance in Medicine*, Vol. 32, no. 6, pp. 707–713, 1994.

50. Wedeen, V. J., P. Hagmann, W.-Y. I. Tseng, T. G. Reese, and R. M. Weisskoff, "Mapping complex tissue architecture with diffusion spectrum magnetic resonance imaging," *Magnetic Resonance in Medicine*, Vol. 54, no. 6, pp. 1377–1386, 2005.

51. Tuch, D. S., T. G. Reese, M. R. Wiegell, N. Makris, J. W. Belliveau, and V. J. Wedeen, "High angular resolution diffusion imaging reveals intravoxel white matter fiber heterogeneity," *Magnetic Resonance in Medicine*, Vol. 48, no. 4, pp. 577–582, 2002.

52. Hess, C. P., P. Mukherjee, E. T. Han, D. Xu, and D. B. Vigneron, "Q-ball reconstruction of multimodal fiber orientations using the spherical harmonic basis," *Magnetic Resonance in Medicine*, Vol. 56, no. 1, pp. 104–117, 2006.

53. Tournier, J.-D., F. Calamante, D. G. Gadian, and A. Connelly, "Direct estimation of the fiber orientation density function from diffusion-weighted mri data using spherical deconvolution," *NeuroImage*, Vol. 23, no. 3, pp. 1176 – 1185, 2004.

54. Özarslan, E., T. M. Shepherd, B. C. Vemuri, S. J. Blackband, and T. H. Mareci, "Resolution of complex tissue microarchitecture using the diffusion orientation transform (DOT)," *NeuroImage*, Vol. 31, no. 3, pp. 1086 – 1103, 2006.

55. Alexander, D., G. Barker, and S. Arridge, "Detection and modeling of non-gaussian apparent diffusion coefficient profiles in human brain data," *Magnetic Resonance in Medicine*, Vol. 48, no. 2, pp. 331–340, 2002.

56. Tournier, J.-D., F. Calamante, D. G. Gadian, and A. Connelly, "Improved probabilistic streamlines tractography by 2nd order integration over fibre orientation distributions," in *Proceedings of the International Society for Magnetic Resonance in Medicine*, p. 1670, 2010.

57. Smith, R. E., J.-D. Tournier, F. Calamante, and A. Connelly, "SIFT: Spherical-deconvolution informed filtering of tractograms," *NeuroImage*, Vol. 67, pp. 298 – 312, 2013.

58. Willats, L., D. Raffelt, R. E. Smith, J.-D. Tournier, A. Connelly, and F. Calamante, "Quantification of track-weighted imaging (TWI): Characterisation of within-subject reproducibility and between-subject variability," *NeuroImage*, Vol. 87, pp. 18 – 31, 2014.

59. Caruyer, E., A. Daducci, M. Descoteaux, J.-C. Houde, J.-P. Thiran, and R. Verma, "Phantomas: a flexible software library to simulate diffusion MR phantoms," in *ISMRM*, (Milan, Italy), May 2014.

60. Uluğ, A. M., M. Ozkan, , P. B. Kingsley, I. De Lucia, A. Celik, P. DeRosse, A. Malhotra, and P. R. Szeszko, "Multi-contrast z-score comparison discriminates patients with psychiatric disorders from controls," *Proc. Intl. Soc. Mag. Reson. Med.*, Vol. 23, p. 3561, 2015.

61. Jenkinson, M., C. F. Beckmann, T. E. Behrens, M. W. Woolrich, and S. M. Smith, "Fsl," *NeuroImage*, Vol. 62, no. 2, pp. 782 – 790, 2012.

62. Smith, S. M., "Fast robust automated brain extraction," *Human Brain Mapping*, Vol. 17, no. 3, pp. 143–155, 2002.

63. Vercauteren, T., X. Pennec, A. Perchant, and N. Ayache, "Non-parametric diffeomorphic image registration with the demons algorithm," in *MICCAI'07*, pp. 319–326, Berlin, Heidelberg: Springer, 2007.

64. Jeurissen, B., J.-D. Tournier, T. Dhollander, A. Connelly, and J. Sijbers, "Multi-tissue constrained spherical deconvolution for improved analysis of multi-shell diffusion mri data," *NeuroImage*, Vol. 103, no. Supplement C, pp. 411 – 426, 2014.

65. Oishi, K., A. V. Faria, P. C. M. van Zijl, and S. Mori, *MRI Atlas of Human White Matter*, Amsterdam, The Netherlands: Elsevier, 2005.

66. Burhans, L., A. Talk, and M. Gabriel, "Cingulate cortex," in *International Encyclopedia of the Social & Behavioral Sciences* (Smelser, N. J., and P. B. Baltes, eds.), pp. 1799 – 1805, Oxford: Pergamon, 2001.

67. Maier-Hein, K. H., P. F. Neher, and J.-C. Houde et.al., "The challenge of mapping the human connectome based on diffusion tractography,"

68. Civier, O., R. E. Smith, C.-H. Yeh, A. Connelly, and F. Calamante, "Is removal of weak connections necessary for graph-theoretical analysis of dense weighted structural connectomes from diffusion mri?," *NeuroImage*, Vol. 194, pp. 68 – 81, 2019.

69. Pasternak, O., S. Kelly, V. J. Sydnor, and M. E. Shenton, "Advances in microstructural diffusion neuroimaging for psychiatric disorders," *NeuroImage*, Vol. 182, pp. 259 – 282, 2018. Microstructural Imaging.

70. Anticevic, A., X. Hu, Y. Xiao, J. Hu, F. Li, F. Bi, M. W. Cole, A. Savic, G. J. Yang, G. Repovs, J. D. Murray, X.-J. Wang, X. Huang, S. Lui, J. H. Krystal, and Q. Gong, "Early-course unmedicated schizophrenia patients exhibit elevated prefrontal connectivity associated with longitudinal change," *Journal of Neuroscience*, Vol. 35, no. 1, pp. 267–286, 2015.

71. Manoach, D. S., R. L. Gollub, E. S. Benson, M. M. Searl, D. C. Goff, E. Halpern, C. B. Saper, and S. L. Rauch, "Schizophrenic subjects show aberrant fmri activation of dorsolateral prefrontal cortex and basal ganglia during working memory performance," *Biological Psychiatry*, Vol. 48, no. 2, pp. 99 – 109, 2000.

72. Whittaker, J. R., S. F. Foley, E. Ackling, K. Murphy, and X. Caseras, "The functional connectivity between the nucleus accumbens and the ventromedial prefrontal cortex as an endophenotype for bipolar disorder," *Biological Psychiatry*, Vol. 84, no. 11, pp. 803 – 809, 2018. Bipolar Disorder: Emerging Pathophysiologic Mechanisms.

73. Türe, U., M. G. Yaşargil, and T. G. Pait, "Is There a Superior Occipitofrontal Fasciculus? A Microsurgical Anatomic Study," *Neurosurgery*, Vol. 40, pp. 1226–1232, 06 1997.

74. Meola, A., A. Comert, F.-C. Yeh, L. Stefaneanu, and J. C. Fernandez-Miranda, "The controversial existence of the human superior fronto-occipital fasciculus: Connectome-based tractographic study with microdissection validation," *Human Brain Mapping*, Vol. 36, no. 12, pp. 4964–4971, 2015.

75. Bao, Y., Y. Wang, W. Wang, and Y. Wang, "The superior fronto-occipital fasciculus in the human brain revealed by diffusion spectrum imaging tractography: An anatomical reality or a methodological artifact?," *Frontiers in Neuroanatomy*, Vol. 11, p. 119, 2017.

76. Sarrazin, S., C. Poupon, J. Linke, M. Wessa, M. Phillips, M. Delavest, A. Versace, J. Almeida, P. Guevara, D. Duclap, E. Duchesnay, J.-F. Mangin, K. Le Dudal, C. Daban, N. Hamdani, M.-A. D'Albis, M. Leboyer, and J. Houenou, "A Multicenter Tractography Study of Deep White Matter Tracts in Bipolar I Disorder: Psychotic Features and Interhemispheric Disconnectivity," *JAMA Psychiatry*, Vol. 71, pp. 388–396, 04 2014.

77. Tuozzo, C., A. E. Lyall, O. Pasternak, A. C. James, T. J. Crow, and M. Kubicki, "Patients with chronic bipolar disorder exhibit widespread increases in extracellular free water," *Bipolar Disorders*, Vol. 20, no. 6, pp. 523–530, 2018.

78. Bracht, T., S. Steinau, A. Federspiel, C. Schneider, R. Wiest, and S. Walther, "Physical activity is associated with left corticospinal tract microstructure in bipolar depression," *NeuroImage: Clinical*, Vol. 20, pp. 939 – 945, 2018.

79. Szeszko, P. R., E. T. Tan, A. M. Uluğ, P. B. Kingsley, J. A. Gallego, K. Rhindress, A. K. Malhotra, D. G. Robinson, and L. Marinelli, "Investigation of superior longitudinal fasciculus fiber complexity in recent onset psychosis," *Progress in Neuro-Psychopharmacology and Biological Psychiatry*, Vol. 81, pp. 114 – 121, 2018.

80. Wu, Y., D. Sun, Y. Wang, Y. Wang, and S. Ou, "Segmentation of the cingulum bundle in the human brain: A new perspective based on dsi tractography and fiber dissection study," *Frontiers in Neuroanatomy*, Vol. 10, p. 84, 2016.

81. Jones, D., K. Christiansen, R. Chapman, and J. Aggleton, "Distinct subdivisions of the cingulum bundle revealed by diffusion mri fibre tracking: Implications for neuropsychological investigations," *Neuropsychologia*, Vol. 51, no. 1, pp. 67 – 78, 2013.

82. Rolls, E. T., C.-C. Huang, C.-P. Lin, J. Feng, and M. Joliot, "Automated anatomical labelling atlas 3," *NeuroImage*, Vol. 206, p. 116189, 2020.

83. Yushkevich, P. A., J. Piven, H. C. Hazlett, R. G. Smith, S. Ho, J. C. Gee, and G. Gerig, "User-guided 3d active contour segmentation of anatomical structures: Significantly improved efficiency and reliability," *NeuroImage*, Vol. 31, no. 3, pp. 1116 – 1128, 2006.

84. Wassermann, D., L. Bloy, E. Kanterakis, R. Verma, and R. Deriche, "Unsupervised white matter fiber clustering and tract probability map generation: Applications of a Gaussian process framework for white matter fibers," *NeuroImage*, Vol. 51, pp. 228–241, 2010.